Glacio-eustatic variations and Sapropel events as main controls on the Middle Pleistocene-Holocene evolution of the Cabliers Coral Mound Province (W Mediterranean)

Guillem Corbera[a,b], Claudio Lo Iacono[c], Christopher D. Standish[b], Eleni Anagnostou[d], Jürgen Titschack [e,f], Orestis Katsamenis[g], Isabel Cacho[h], David Van Rooij[i], Veerle A.I. Huvenne[a], Gavin L. Foster[b]

[a] National Oceanography Centre, Southampton, United Kingdom

[b] School of Ocean and Earth Science, National Oceanography Centre Southampton, University of Southampton, SO14 3ZH, United Kingdom

[c] Institut de Ciències del Mar (CSIC), Passeig Marítim de la Barceloneta, 08003 Barcelona, Spain..

[d] GEOMAR Helmholtz Centre for Ocean Research, Kiel, Germany

[e] MARUM Centre for Marine Environmental Sciences, University of Bremen, Germany

[f] Senckenberg am Meer, Marine Research Department, 26382 Wilhelmshaven, Germany

[g] University of Southampton, m-VIS X-Ray Imaging Centre, Faculty of Engineering and the Environment, SO17 1BJ Southampton, United Kingdom.

[h] University of Barcelona, Barcelona, Spain.

[i] Ghent University, Department of Geology, Belgium

ABSTRACT

Cold-water coral mounds are key hot-spots of deep ocean biodiversity and also important archives of past climatic conditions. Nonetheless, the paleo-oceanographic setting in which coral mounds developed in the Mediterranean Sea during the last 500 ka still needs to be properly understood. This study describes the coral deposits and corresponding ages of two on-mound gravity cores acquired from opposite sectors of the newly discovered Cabliers Coral Mound Province (CMP, Alboran Sea, W Mediterranean). U-Th data revealed Pleistocene-aged corals covering mound formation periods from >389 to 9.3 ka BP and from 13.7 to 0.3 ka BP in the southern and northern mounds respectively. The

coral-rich deposits of the cores were mainly dominated by *Desmophyllum pertusum,* although in some sections concurrent with the Middle Pleistocene and the Holocene, other corals such as *Dendrophyllia cornigera* and *Madrepora oculata* also appeared as dominating species. Coral mound formation stages generally occurred during deglacials and temperate interstadial (3.5–4.1 δ^{18}O‰) periods, whereas during interglacials (<3.5 δ^{18}O‰) coral mound formation only occurred in the northern and shallower mound. We interpret this to indicate that the shoaling of the interface between Atlantic (AW) and Levantine Intermediate Waters (LIW) during interglacial periods prevented the corals in the southern CMP from acquiring sufficient food supply, thus causing periods of coral mound stagnation. Similarly, the interruption in LIW formation throughout sapropel events also coincides with coral mound stagnation phases. This suggests that sapropel-derived processes, which originated in the eastern Mediterranean, likely affected the entire Mediterranean basin and further supports the role of LIW as a conveyor belt facilitating cold-water coral growth in the Mediterranean Sea. Overall, we show that these coral mounds yield important insights into how local changes in oceanographic conditions can influence coral mound development.

1. INTRODUCTION

With the presence of suitable environmental conditions (e.g. food supply, temperature, salinity, dissolved oxygen, moderate bottom currents) scleractinian cold-water coral (CWC) populations can expand, with new settlement occurring on dead coral framework, and separate coral patches eventually merging to form reefs (Wilson, 1979; De Mol et al., 2005; Roberts el al., 2006; Lo Iacono et al., 2018). Such reefs consist of a bio-constructed three-dimensional framework composed of living and dead CWCs, which provides a range of ecological niches for the settlement of many species (Roberts et al., 2006; Price et al., 2019). Although most studied CWC reefs are commonly formed by *Desmophyllum pertusum* (synonym = *Lophelia pertusa*; Addamo et al., 2016), other framework-building CWCs such as *Madrepora oculata*, *Enallopsammia profunda, Solenosmilia variabilis* and *Oculina varicosa* can also form reefs on their own (Reed et al., 1980; Roberts et al., 2006; Raddatz et al. 2020). The complex structure of CWC reefs increases turbulence and reduces the current speeds among the corals, thus trapping hemipelagic sediments (Hebbeln et al., 2016). The latter, in turn, help to stabilise the coral framework, preventing its physical collapse when the coral colonies become too large (De Mol et al., 2002; Dorschel et al., 2005; Wienberg and Titschack, 2017). Over geological timescales, if suitable environmental conditions persist, CWC reefs can grow and form prominent geomorphological structures, known as coral mounds (Roberts et al., 2006, 2009; Wienberg and Titschack, 2017; Lo Iacono et al., 2018).

Coral mounds generally occur in clusters and they are mainly described from the Northeast Atlantic margin, within a depth range of 70–1200 m (Wheeler et al., 2007; Lo Iacono et al 2018). However, in the last decade new coral mound provinces have also been discovered off the west-African coast (Eisele et al., 2011, 2014; Van Dorpe et al., 2017; Wienberg et al., 2018; Tamborrino et al., 2019), the eastern continental slopes of North and South America (Grasmueck et al., 2006; Raddatz et al., 2020) and in the Mediterranean Sea (Comas and Pinhero, 2010; Lo Iacono et al., 2014, 2016; Savini and Corselli, 2010; Corbera et al., 2019). Regardless of where they occur, CWC mounds present a wide range of sizes and shapes (Lo Iacono et al., 2018). From conical mini-mounds that are a few metres tall (e.g. Darwin and Moira Mounds; Bett et al., 2001; Foubert et al., 2011) to giant ridge-like mounds that rise hundreds of meters above the surrounding seafloor (e.g. Challenger Mound and Brittlestar mounds; Kano et al., 2007; Comas and Pinheiro, 2010; Fink et al., 2013). Such mound morphologies are sometimes associated with the presence of a geological structure on which the corals first settled and started to grow (Lo Iacono et al., 2014, 2018; Hebbeln, 2019). Nevertheless, persistent current dynamics

can also have an effect on the shape of growing coral mounds (Huvenne et al., 2003; López-Correa et al., 2012; Hebbeln et al., 2014; Buhl-Mortensen et al., 2016).

Coral mound development can last from a few thousand up to millions of years (Kano et al., 2007; Frank et al., 2011; Victorero et al., 2016). Over this time, paleo-climatic fluctuations such as glacial-interglacial cycles occurred, involving drastic changes in relative sea-level (RSL), seawater temperature and many other environmental variables, including surface productivity and water oxygenation (Dorschel et al., 2005; Roberts et al., 2006; Thierens et al., 2013). These variations exert a strong control on the increase, reduction and stagnation of coral mound formation, in some cases even producing winnowing and mass-wasting of their exposed portion (López-Correa et al., 2012; Stalder et al., 2015; Tamborrino et al., 2019). Environmental variations experienced during coral mound formation can be recorded in the skeletons of growing corals as the concentration and isotopic composition of certain elements (e.g. Li, Mg, U, Ba, B, Nd) that reflect the local physicochemical parameters of the surrounding water (Montagna et al., 2014; Spooner et al., 2018). As paleoclimatic archives, absolutely dated CWCs combined with the extraction of geochemical proxies and computed tomography scans can thus give highly relevant information on coral mound development and its paleo-climatic constrains (Fink et al., 2013; Raddatz et al., 2016; Montagna and Taviani, 2019; Wang et al., 2019).

In the Mediterranean basin, CWC mound provinces tend to occur together with contourite deposits (Rebesco and Taviani, 2019) and are concentrated in the Ionian Sea (Savini and Corselli, 2010; Savini et al., 2014), the Thyrrhenian Sea (Remia and Taviani, 2005; Angeletti et al., 2020) and the Alboran Sea, this last being the only basin where mounds reach sizes of >100 m in height and several kilometres in length (Comas and Pinhero, 2010; Fink et al., 2013; Lo Iacono et al., 2014, 2016; Corbera et al., 2019). Several studies have attempted to link coral mound growth patterns in the Alboran Sea to different environmental factors, in order to better understand what are the main processes driving or limiting CWC mound development in the region (Fink et al., 2013; Lo Iacono et al., 2014; Fink et al., 2015; Stalder et al., 2015; Wang et al., 2019). Fink et al. (2013, 2015) linked coral mound formation in the Alboran Sea to periods of enhanced productivity and increased water mass circulation, while Wang et al. (2019) suggested that mound formation is controlled by a complex interplay between productivity and changes in the relative sea-level, which affected the depth of the interface between Atlantic and Mediterranean water masses. Despite the great amount of knowledge won, none of these studies have been able to investigate CWC mound development beyond the last 15 kyr. Therefore, knowledge on coral mound development prior to the Bølling-Allerød (B/A; i.e. >15 ka BP) is minimal, which impedes

115   a more comprehensive description of Mediterranean coral mound development in response to Late

116   Quaternary paleo-climatic changes in the area.

117

118   This study describes the coral deposits and corresponding ages of two on-mound gravity cores collected

119   from opposite ends of the recently discovered Cabliers Coral Mound Province (hereafter as CMP; Fig.

120   1; Lo Iacono et al., 2016). Previous studies have shown that while CWCs thrive on the northernmost

121   sector of the CMP, the corals on its southern end are dead (Corbera et al., 2019). This change in CWC

122   abundance observed between the two ends of the province (15 km apart), most probably reflects

123   differences in the existing local environmental conditions (i.e. hydrodynamics, physicochemical

124   conditions of the water, food supply; Corbera et al., 2019), which makes this mound province an ideal

125   setting for the study of coral mound evolution in response to local and regional environmental changes.

126   Thus, with the general purpose of acquiring a better understanding of coral mound development in the

127   Mediterranean Sea, this study aims to (1) describe the temporal development of the northern and

128   southern sectors of the CMP during the last ~500 ka BP, (2) relate the changes in mound growth patterns

129   to paleo-climatic events that modified the regional and local environmental setting and (3) compare the

130   paleo-evolution of the CMP with the mound development patterns of already studied coral mound

131   provinces, specifically in the Alboran Sea.

132

133   2. STUDY AREA

134

135   The Alboran Sea is the westernmost basin of the Mediterranean Sea, bound by the Iberian Peninsula to

136   the north and Northern Africa to the south (Fig. 1B). To the west, the Strait of Gibraltar connects this

137   basin to the Atlantic Ocean, while to the east the boundary of the Alboran Sea is defined by the area

138   connecting Cabo de Gata (Spain) with Cap Figalo (Algeria) (Fig. 1B). The Alboran Sea displays a

139   complex seafloor geomorphology, which exhibits several seamounts, volcanic banks and ridges.

140   (Duggen et al., 2004; Lo Iacono et al., 2008; Palomino et al., 2015).

141
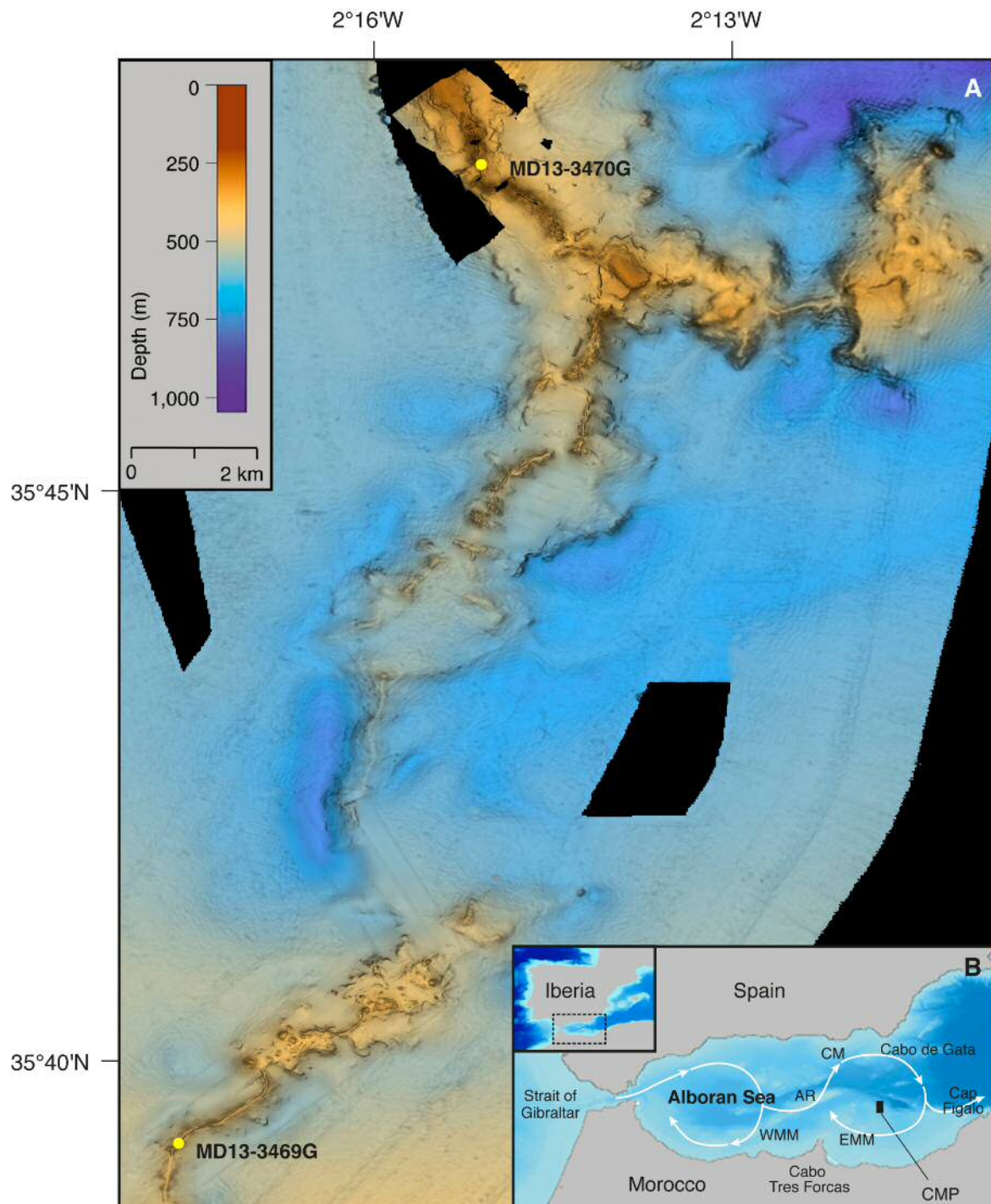
Figure 1. Shipboard multi-beam bathymetric model (20 m resolution) of the Cabliers Coral Mound Province (CMP) (A). Inset of the Alboran Sea, with the black rectangle indicating the location of the CMP (B). The yellow dots in (A) show the location of both MD13-3469G and MD13-3470G. AR: Alboran Ridge, CM: Chella Mound (Lo Iacono et al., 2018), WMM: West Melilla Mounds (Lo Iacono et al., 2014), EMM: East Melilla Mounds (Comas and Pinheiro, 2010). White arrows: surface Atlantic Water circulation.

Ocean circulation patterns within the Alboran Sea are largely driven by the interaction between the Atlantic Water (AW), entering from the west, and the Levantine Intermediate Water (LIW) and West Mediterranean Deep Water (WMDW), flowing in from the east. This creates a small-scale thermohaline

circulation (Garcia Lafuente et al., 1998). The AW is the main driver of the surface circulation in the Alboran Sea and consists of warmer and fresher waters (T~15°C, S~36.2, Ba_{SW} ~40 nmol/kg) that flow towards the east from the surface down to 150-200 m deep (Garcia Lafuente et al., 1998; Vargas-Yañez et al., 2017; Roy-Barman et al., 2019). Below the AW, the colder and more saline waters of the LIW (T~13.2°C, S~38.5, Ba_{SW} ~70 nmol/kg) flow much slower in opposite direction at 200-600 m water depth (Roy-Barman et al., 2019). The LIW is a water mass that originates in the Eastern Mediterranean Basin and spreads across the southern sector of the Western Mediterranean towards the Alboran Sea, where it flows out to the Atlantic Ocean and contributes to the formation of the Mediterranean Outflow Water (MOW) (Millot, 2009). Finally, the WMDW (T~12.9°C, S~38.4, Ba_{SW} ~75 nmol/kg), which is a deep water mass formed in the Gulf of Lions, flows beneath the LIW down to the seafloor, following the same direction and also contributing to the MOW's formation (Vargas-Yañez et al., 2017; Roy-Barman et al., 2019).

The interaction between Atlantic and Mediterranean waters together with the geomorphology of the Alboran Basin sustains a system of two semi-permanent anticyclonic gyres, the stability and intensity of which depend on the amount of AW coming through the Strait of Gibraltar (Vargas-Yáñez et al., 2002). The western quasi-permanent gyre is located between the Strait of Gibraltar and Cabo Tres Forcas, whereas the eastern and more variable gyre is found in between Cabo Tres Forcas and Cap Figalo (Fig. 1). Both gyres are active during summer, while in winter only the western anticyclonic gyre prevails (Vargas-Yáñez et al., 2002; Macías et al., 2008). Overall, the gyre system stimulates the formation of upwelling areas that bring nutrients up to shallower waters, which increase the primary productivity at the surface and makes the Alboran Sea the most productive region within the Mediterranean Sea, with 200–300 gC m^{-2} a^{-1} (Bosc et al., 2004; Oguz et al., 2014). Such productivity mostly accumulates in a meandering jet of AW that flows into the Alboran Sea following the course of the two anticyclonic gyres (Navarro et al., 2011; Oguz et al., 2014). Moreover, it is known that in the Alboran Sea, around 250 m water depth and close to the interface between AW and LIW, diurnal frequency internal waves occur (Van Haren, 2014).

In this basin, coral mounds are distributed into three main provinces: the West Melilla Mounds (WMM), the East Melilla Mounds (EMM; Fig. 1B) and the CMP. The WMM consists of 103 conical-shaped mounds up to 48 m tall and 476 m in diameter, in a depth range of 298–590 m but with no living corals currently occurring on the mounds (Lo Iacono et al., 2014). The EMM are composed of >30 ridge-like mounds that can extend for >15 km and reach 150 m in height, in a depth range of 200–475 m (Hebbeln, 2019). In this province living CWCs are not common and only appear as small scattered colonies at the mounds' crests (Hebbeln et al., 2009). The CMP is located ~40 km northeast of the EMM, it extends NE-SW for 25 km and is mainly formed by ridge-like mounds with an average height of 77 m, in a depth range of 250–710 m (Fig. 1). In contrast to what is known for the rest of coral mound provinces

191 in the Mediterranean Sea, ROV footage has revealed large thriving CWC reefs occurring on the summit

192 of the CMP northernmost sector (Corbera et al., 2019).

193

194 3. MATERIAL AND METHODS

195

196 **3.1. Core acquisition and analyses**

197

198 The two gravity cores (MD3469G and MD3470G) used for this study were collected from the summit

199 of two coral mounds, located on opposite ends of the CMP, in June 2013 during the Eurofleets

200 "GATEWAY" Cruise MD194, onboard the R/V Marion Dufresne (Table 1). Core MD13-3470G was

201 retrieved from 313 m water depth at the northernmost part of the CMP. In contrast, core MD13-3469G

202 was extracted from 417 m water depth, 15 km further to the south-west. The gravity corer managed to

203 recover 8.40 and 10.38 m of core material for MD3470G and MD3469G respectively, consisting of

204 dense coral framework and coral rubble embedded in hemipelagic sediments. The cores were cut in 1

205 m sections, scanned through high-resolution computed tomography and frozen before being split. The

206 1 m long sections were split while frozen using a diamond rock saw, to minimize coral fragmentation

207 during cutting operations. The sections were then defrosted and HD photographed employing the

208 Geotek MSCL-Core Imaging System from the British Ocean Sediment Core Research Facility

209 (BOSCORF). The two cores were visually logged.

210

211 **Table 1.** MD13-3469G and MD13-3470G core location, water depth and recovery. Number of samples
212 for Uranium series and geochemical proxies is indicated, together with the youngest and oldest samples
213 of each core.

Core	Lat	Long	Water depth (m)	Recovery (m)	U-Th samples	Li/Mg and Ba/Ca samples	Age (ka BP) Min.	Age (ka BP) Max.
MD13-3469G	35°39.409'N	2°17.731'W	417	10.38	59	24	9.3	588.9
MD13-3470G	35°47.755'N	2°15.152'W	313	8.4	51	10	0.3	13.7

214

215

216 **3.2. Computed tomography scans**

217

218 Prior to splitting, the ~1m gravity core sections were scanned in sections of 10 cm at the μ-Vis facilities

219 of the University of Southampton, using a custom built, dual source 225/450 kV walk-in room CT

220 scanner (Nikon Metrology, UK). To acquire the scans, the microfocus 450 kV source was fitted with a

221 tungsten reflection target together with a Perkin Elmer XRD 1621 CN03 HS detector. Projections were

222 acquired during a full 360º rotation. Images were then reconstructed, resulting in an isotropic voxel-

223 size of 71.4 μm. However, voxel resolution was later down-sampled to 200 μm in order to facilitate a

224 more efficient data handling and analysis. Later, the image processing software Fiji was used to apply

225 an anisotropic diffusion filter (default settings) to reduce the noise in the scans, while keeping detail in

226 sharp edges. All further processing was performed with the ZIB edition of the Amira software (version

227 2018.04; Stalling et al., 2005; http://amira.zib.de). The 10 cm volumes were fused into 1 m sections,

228 using the intensity of the core liner to calibrate the variation in intensity of the sediments and the corals
229 between neighbouring volumes. Watershed segmentation was used to segment the macroscopic (>1
230 mm) carbonate fragments, dominated by CWCs, from the sediment. The volumetric percentage of
231 CWCs in each CT slice was quantified with the *MaterialStatistics* module (Volume per slice). The
232 *ContourTreeSegmentation* module was subsequently employed to achieve an automatic segmentation
233 and separation of neighbouring clasts. The resulting 3D reconstruction of the bigger coral fragments
234 (>20 mm) was used to visually identify the dominating coral species along the core. Finally, coral
235 preservation patterns (CPP) were defined through the quantification of clast size and inclination by
236 means of the *ShapeAnalysis* module. In some cases, the transition section between CPPs is marked by
237 an abrupt variation in different macroscopic parameters (e.g. coral content (vol. %), clast size and
238 inclination, presence of Fe-Mn coated corals and species dominance; hereafter referred to as an
239 unconformity), which suggests that changes in the environmental setting caused a substantive
240 modification in the coral mound development.
241
242 **3.3. Grain size analysis**
243
244 In total, 53 and 45 sediment samples from the cores MD3469G and MD3470G were collected every 20
245 cm and dried at 80°C for 24 hours. The samples where then placed in a solution of H_2O_2 20% for 15
246 days in order to remove all the organic matter. Subsequently, they were subjected for 24 hours to the
247 action of a dispersant (i.e. sodium polyphosphate 40 ml l^{-1}) to separate the grains. Once the preparation
248 of the samples was finished the coarser fraction was sieved for 6000, 4000 and 2000 μm. Finally, the
249 total sediment fraction finer than 2000 μm was examined using an LA-950V2 laser scattering particle
250 size distribution analyser (HORIBA) at the Institute of Marine Sciences (ICM-CSIC), which detects
251 grains down to 0.031 μm.
252
253 **3.4. Uranium series absolute dating**
254
255 59 and 51 coral fragments were extracted from the cores MD3469G and MD3470G respectively to be
256 dated through uranium series techniques at the University of Southampton (Table 1). Four coral
257 fragments from each core, were dated via solution multi-collector inductively coupled plasma mass
258 spectrometry (MC-ICP-MS) to provide accurate and precise temporal constraints for both cores. All
259 other samples were dated through laser ablation MC-ICP-MS (Spooner et al. 2016). Four of the samples
260 analysed by solution were split in two pieces before processing to provide internal reference materials
261 for laser ablation MC-ICP-MS.
262
263 Given that some samples were analysed by both solution and LA techniques, with LA samples being
264 analysed either singularly or multiple times, ages were prioritised in the following manner when
265 assessing coral growth: 1) solution MC-ICP-MS analyses (Table A1), 2) mean (± 2 SD) LA-MC-ICP-
266 MS ages of multiple analyses (Table A2), and 3) single LA-MC-ICP-MS analysis (Table A2).

The final ages were used to calculate the aggradation rates (ARs) of the different coral mound formation periods. We associated the oldest and youngest ages of each mound formation period to the deepest and shallowest samples of such period respectively. This method provides conservative AR estimations for each mound formation period.

3.4.1. Solution U-Th dating

Coral fragments were cut into small samples (0.12–0.3 g) using a circular saw. Organic matter and possible Fe-Mn crusts were mechanically and chemically cleaned, following a procedure similar to the one published by Cheng et al. (2000). This protocol consisted of a succession of ultra-sonication steps with 18.2 MΩ cm (ultrapure) H_2O, oxidative and reductive solutions, intercalated with washes of the samples. The samples were then dissolved by stepwise addition of concentrated HNO_3 (~15.5 N). The separation of U and Th from the sample matrix was performed by ion exchange chromatography, employing 0.6 ml columns and 100–150 µm UTEVA Spec (Eichrom) resin (Horwitz et al., 1992) and following the method published in Hoffmann et al. (2018) for the University of Southampton geochemistry facilities. The U and Th isotope measurements were undertaken on a Neptune Plus MC-ICP mass spectrometer (Thermo Fisher Scientific, Waltham, MA, USA) equipped with nine Faraday cup detectors and an energy filter (Retarding Potential Quadrupole lens) on the central ion counter. All analytical procedures and calculations were undertaken following the methods in Hoffman et al. (2007; 2018). For the calculation of activity ratios the following decay constants were used: λ_{230} = $(9.1577\pm0.028)\cdot10^{-6}$ a^{-1} (Cheng et al. 2000), λ_{232} = $(4.94752\pm0.035)\cdot10^{-11}$ a^{-1} (Holden 1990), λ_{234} = $(2.826\pm0.0056)\cdot10^{-6}$ a^{-1} (Cheng et al. 2000), and λ_{238} = $(1.55125\pm0.0017)\cdot10^{-10}$ a^{-1} (Jaffey et al. 1971). Ages were calculated iteratively from the activity ratios and using the above half-lives. Following Scholz et al. (2004), corrections for initial Th assume a $(^{232}Th/^{238}U)_A$ value typical of upper crustal silicates (Wedepohl, 1995): 1.250±0.625 (whilst assuming ^{230}Th and U isotopes are in equilibrium).

Long-term accuracy and external reproducibility of solution U-Th dating was demonstrated through repeat analyses of a secular equilibrium standard, uraninite URAN 84.5, over a period of 4 years (detailed in Supplementary Data).

3.4.2. Laser ablation U-Th dating

Samples and standards for laser ablation analyses were mounted in epoxy resin (2.5 cm diameter disks) and polished until the surface of the resin was flat, and the samples were exposed. The analyses were performed at the University of Southampton, using an Elemental Scientific Lasers (Bozeman, MT, USA) NWR193 excimer laser ablation system with a TwoVol2 ablation chamber coupled to a Thermo Scientific Neptune Plus MC-ICP-MS.

A peak hopping approach between two sub-configurations, based on 'Procedure 2' of Spooner et al. (2016), was employed using VS001/1-A, a fragment of inorganically precipitated aragonite vein (Kampman et al., 2012), as an aragonite standard (detailed in Supplementary Data): ^{230}Th and ^{234}U intensities were measured using the central ion counter whilst ^{238}U intensities were measured using Faraday cups (see Table A3). Integration times were 4.194 s and idle times were 1 s for both sub-configurations, giving a total cycle time of 10.388 s. Spooner et al. (2016) demonstrated that measuring ^{232}Th for correction of initial Th was not necessary in most cases when analysing CWCs. Analyses of ^{232}Th was therefore not included in the approach employed here, a decision that is validated by the accuracy of the internal standards discussed below. Typical operating conditions are detailed in Table A4. To remove any surface contamination, coral samples were pre-ablated prior to analyses. Rather than ablating a single spot, laser ablation was carried out along a straight line on the sample surface. This method keeps a steadier signal intensity and inter-element fractionation compared to spot analyses (Spooner et al., 2016).

Activity ratios and age calculations were performed in the same way as outlined in section 3.4.1. The number of samples analysed in one run was limited to 40 in order to avoid decreased sensitivity due to carbonate build up on the skimmer and sampler cones. Furthermore, some of the samples found at the initiation or end of an intense coral mound growth period were dated repeatedly (5 measurements) to reach a more precise average age through replication and thus achieve a better constrained picture of mound development.

Accuracy of the laser ablation MC-ICP-MS is demonstrated through analyses of four coral samples also analysed by solution MC-ICP-MS (Table A3 and Fig. A1). These four samples, alongside a further 12, were analysed multiple times throughout the period of study to demonstrate the external reproducibility of the approach. Expressed as 2 standard deviations (SD) of the mean of the multiple analyses, these range from 20.8 % to 1.2 % for (^{230}Th/^{238}U) equal to 0.03 and 1.25 respectively, and are $\leq$2 % for (^{234}U/^{238}U). External reproducibility at 95% confidence of calculated U-Th ages range from±0.5 ka for an age of 2.8 ka (16.8 %) to±26.8 ka for an age of 316.3 ka (8.6 %); comparable to previous studies using laser ablation MC-ICP-MS (Eggins et al., 2005; McGregor et al., 2011; Spooner et al., 2016). External reproducibility of the δ^{234}U$_i$ is typically better than 25 ‰ (2 SD). Spooner et al. (2016) discussed the factors contributing to the external reproducibility of the calculated laser ablation ages in some detail and demonstrated that it is possible to estimate the reproducibility of the age of any sample based on its (^{230}Th/^{238}U). This approach is followed here, where age uncertainty is determined based on the relationship between the external reproducibility of those samples analysed multiple ($\geq$3) times and their (^{230}Th/^{238}U) (Fig. A2). These give calculated uncertainties (at 95% confidence) of ~0.7 ka for ages of 0–10 ka, ~0.9 ka for ages of ~15 ka, ~5 ka for ages of 100 ka, and ~19 ka for ages of ~350 ka. This approach could not characterise uncertainty on samples >400 ka, therefore such samples were not considered during dating discussions.

3.5. Trace elements analyses

From the dated coral fragments, 24 individuals from core MD3469G and 10 from core MD3470G were further processed for Li/Mg and Ba/Ca analyses. The Li/Mg ratio in CWCs relates to the seawater temperature in which the corals grew (e.g. Case et al., 2010; Montagna et al., 2014; Stewart et al., 2020). Ba/Ca ratios are linked to seawater Ba concentrations (Ba_{SW}; e.g. Anagnostou et al., 2011; Spooner et al., 2018), which can be used to trace different water masses and changes in terrigenous input (Roy-Barman et al., 2019). The corals were first mechanically cleaned using a circular saw, to remove any Fe-Mn crust and visible borings, and then ultra-sonicated several times to remove any lose sediments trapped within the coral features. Subsequently, the corals were subjected to oxidative and reductive cleaning, to remove the remaining organic and crustal material, and to dissolution through the use of 0.5M HNO_3 (detailed in Supplementary Data).

The elemental ratios were then measured on the Thermo Element XR (University of Southampton) following established protocols (e.g. Stewart et al., 2017), with a long-term precision (2σ) of consistency standards of 2% for Ba/Ca, and 4% for Li/Mg. To translate elemental ratios into environmental parameters, we used the multispecies calibration of Montagna et al. (2014) on coral Li/Mg ratios to calculate sea water temperatures (SWTs) and the multispecies calibration of Spooner et al. (2018) for reconstructions seawater Ba concentrations. Changes in the Li/Mg ratio in seawater during the last million years are negligible due to the long residence time of Li and Mg in the ocean (Huh et al., 1998). Therefore, it can be assumed that seawater Li/Mg ratios did not change during the timespan encompassed by this study (i.e. ~600 ka). Reconstructions and uncertainties for SWTs and Ba_{SW} were calculated by propagating both the analytical uncertainty of our elemental data and the uncertainty associated to the regression fit of each calibration, refitted here using York (2004), with a Monte Carlo approach (n=1000):

$$Li/Mg \text{ calibration } (\pm 2\sigma): Li/Mg = (5.29\pm0.06) \exp ((-0.046\pm0.001)T),$$
$$Ba/Ca \text{ calibration } (\pm 2\sigma): Ba/Ca = (0.17\pm0.01)Ba_{SW} + (1.9\pm0.7)$$

The values used in all subsequent discussion were the median of the Monte Carlo SWTs and Ba_{SW} realisations for each sample with a 95% confidence derived from the observed 5 and 95% percentiles (Table A5). The Li/Mg-temperature calibration on all biogeogenic aragonites in Stewart et al. (2020) provides indistinguishable SWTs to our approach, including for the extreme estimates.

4. RESULTS

4.1. Cabliers South (Core MD13-3469G)

4.1.1. Visual and CT-based core description

The core MD13-3469G, collected from the southernmost end of the CMP (Fig. 1), consists of 10.38 m of dense CWC framework and coral rubble fragments, within a matrix of fine sediments (Table 1, Fig.

382   2). The sediment matrix consists of olive grey muds interspersed with sporadic calcareous fragments

383   that belong to other invertebrates, such as gastropods, bivalves and echinoids. Visual qualitative logging

384   of the core allowed us to estimate that 41% of its length contains high coral fragment abundance (Fig.

385   2), generally observed in the upper 650 cm (Fig. 2). Similarly, 40% of the core corresponds to more

386   dispersed but still abundant fragments (medium coral abundance in Fig. 2) and 18% to fine sediments

387   with some scattered corals (low coral fragment abundance in Fig. 2). Visual characterisation also helped

388   to detect a small section of the core (1% of core length) dominated by a bivalve facies (561–553 cm;

389   Fig. 2B) and other short sections where the coral fragments were clearly bio-eroded and covered by a

390   ferromanganese crust (863–854 cm and 575–561 cm; Fig. 2B).

391

392   The CT-based coral content (vol.%) oscillates along the core between 1 and 35 vol.% and presents an

393   average value of 15±6 vol.% (Fig. 2). Generally, the change in coral vol.% values matches with the

394   variations in coral abundance observed through visual description of the core halves (Fig. 2). The lowest

395   vol.% values correspond to sections mainly dominated by sediments with scattered corals and to the

396   bivalve facies (Fig. 2B). In contrast, the highest vol.% values relate to sections of the core formed by

397   extremely abundant coral fragments, which mainly consist of *D. pertusum*. A combination of visual and

398   CT-based analyses suggests that the predominant species forming the coral deposits is the framework-

399   building coral *D. pertusum*. This species dominates most of the core, accompanied in some cases by *M.

400   oculata*, *Desmophyllum dianthus* and *Dendrophyllia cornigera*. Yet, in certain sections of the core, *D.

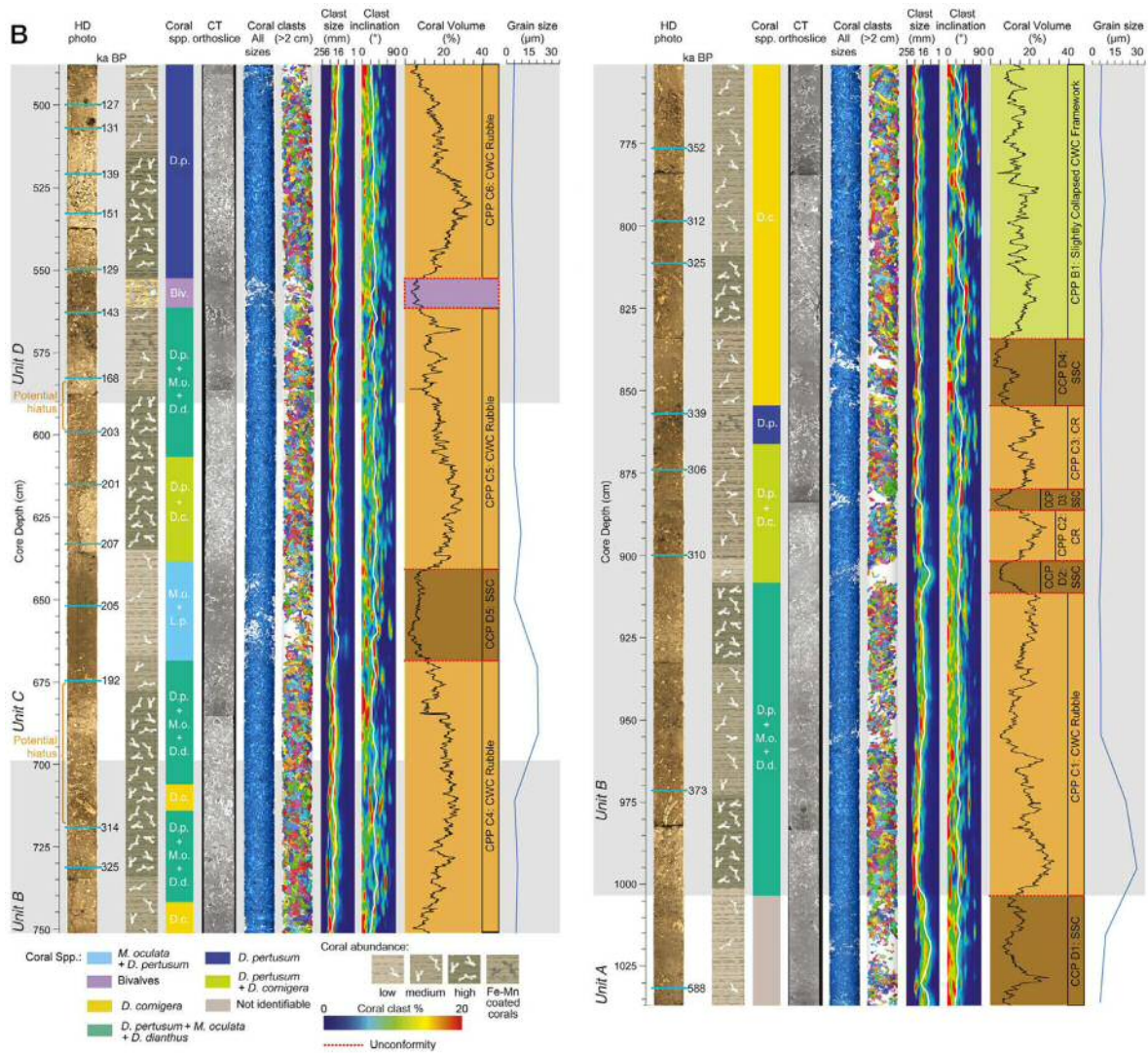401   cornigera* and *M. oculata* dominate the CWC deposits over *D. pertusum* (Figs. 2, 3B).

402

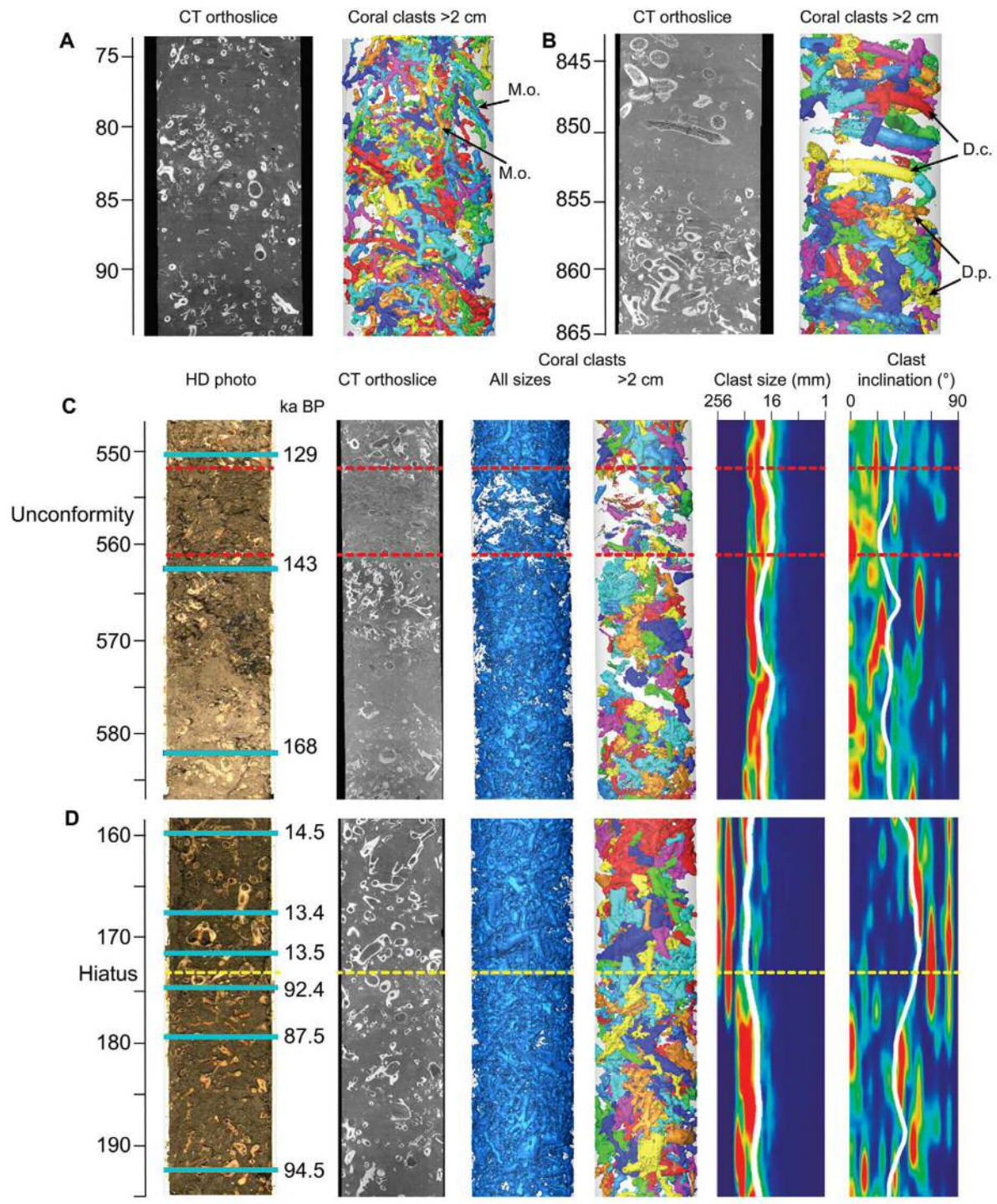403

404
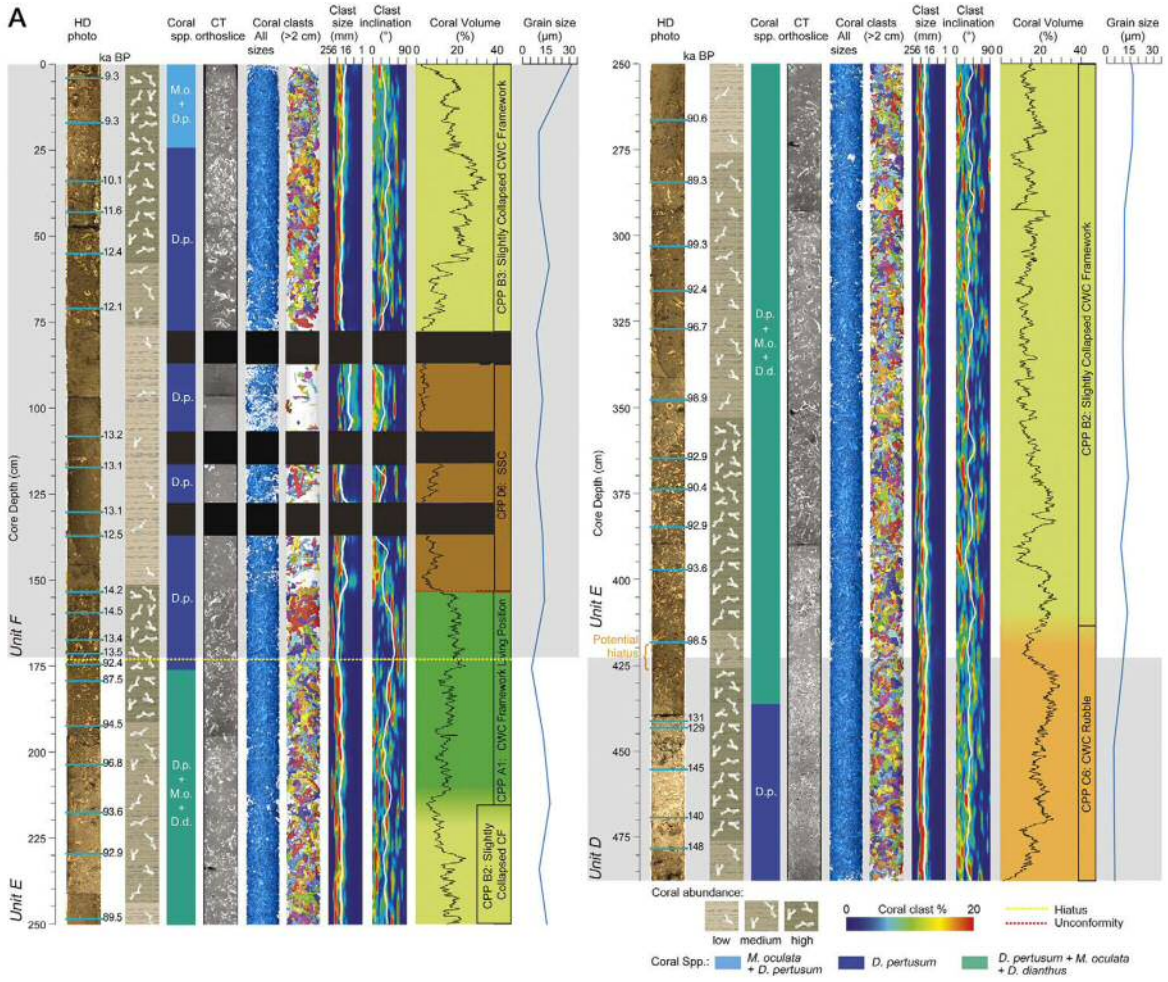
Figure 2. Log of the MD13-3469G core (A: 0–483 cm, B: 483–1038 cm core depth). From left to right: core HD photo with location of the coral samples acquired for uranium series dating (blue lines) and the corresponding ages; stratigraphic representation of coral abundance; changes in the dominating species conforming the coral deposits; raw image of the core CT scans; 3D image of the CT scans including all segmented coral clasts; 3D image of the CT scan including coral clasts >2 cm; coral clast size distribution (white line: mean clast size); coral clast inclination (white line: mean clast inclination); coral volume per slice (200 μm) overprinted on the coral preservation pattern (CPP A-dark green: coral frameworks buried in living position; CPP B-light green: slightly collapsed coral framework; CPP C-orange: coral rubble; CPP D-brown: sediments with scattered coral fragments). The black bands indicate areas with bad quality CT scans that could not be included in the analyses. This figure can be found in supplementary material as four high resolution panels.

15

Figure 3. Detailed CT raw images and coral clasts >2 cm of (A) the uppermost section of core MD13-3470G, dominated by *M. oculata* facies (MO); (B) a section of core MD13-3469G where the coral facies changes from *D. pertusum* (DP) to *D. cornigera* (DC) fragments; and (C, D) detailed core sections of two possible coral mound growth hiatuses in core MD13-3469G. From left to right: Core HD photo with location of the coral samples acquired for uranium series dating (blue lines) and the corresponding ages; raw image of the core CT scans; 3D image of the CT scans including all segmented coral clasts; 3D image of the CT scan including coral clasts >2 cm; coral clast size distribution (white line: mean clast size); coral clast inclination (white line: mean clast inclination).

The CT scan analyses also allowed the identification of four coral preservation patterns (CPPs), defined by different ranges of mean coral clast size and inclination, similar to those described in Titschack et al. (2015): coral framework in sub-vertical living position, slightly collapsed coral framework, coral rubble and sediments with scattered coral fragments. The deposits containing coral framework buried in living position (CPP A) are characterised by a mean coral clast size of >27 mm and variable inclinations, with clear maxima between 70 and 90° (Figs. 2, 5). Slightly collapsed coral framework (CPP B) is defined by average clast sizes ranging between 22.6 and 45.3 mm, and inclinations of <60°. Coral rubble (CPP C) is represented by a coral clast size ranging from 16.0 to 32 mm, and inclinations of <45°. Sediments with scattered coral fragments (CPP D) consists of average coral clasts sizes <16 mm, inclinations of <45°, and average coral content values generally under 10%. The lower half of the core displays coral deposits that mainly consist of coral rubble with sections of sediment with scattered coral fragments (Fig. 2B). In contrast the upper half is mainly dominated by slightly collapsed coral framework deposits, with some rubble and coral frameworks buried in living position (Fig. 2A). Change of CPPs is generally marked by the presence of unconformities (Fig. 2).

Average grain size of the matrix sediment varies from 3.4 µm (clay) to 31.4 µm (medium silt) with a mean value of 10±6.21 µm (Fig. 2). Grain size varies gradually along the core, with values of ~5 µm from 1038 to 450 cm, which increase to ~10 µm up to the top. Only three peaks of 30, 21 and 31.4 µm occur at 995, 690 and 0 cm respectively (Fig. 2). The coarsest grain size value is thus observed at the shallowest point of the core, corresponding with the demise of the mound (Fig. 2A).

To facilitate the description of the change in the species present in the core, the coral preservation patterns and the mound formation stages, the core has been divided in six different units according to the phases of mound development and to the most evident sedimentological features (Fig. 2A, B):

Unit A (1038–1003 cm) – The base of the core consists of mostly unidentified bioclasts (Fig. 2B). This unit is characterised by the dominance of matrix sediments with some scattered coral fragments (CPP D1). Although CPP D1 presents coral volumes over 10% they mainly consist of unidentifiable bioclasts that might not be coral fragments (Fig. 2B).

Unit B (1003–699 cm) – This unit mainly consists of coral rubble (CPP C1:1003–911 cm, CPP C2: 902–887 cm, CPP C3: 880–855 cm, CPP C4: 751–699 cm) and slightly collapsed coral framework (CPP B: 1835–751 cm) combined with small sections of sediments with scattered coral fragments (CPP D2: 911–902 cm, CPP D3: 887–880 cm, CPP D4: 855–835 cm). *D. pertusum* combined with *M. oculata* and *D. dianthus* dominates the coral deposits from 1003 to 902 cm. From 902 to 685 cm, *D. cornigera* is present among the coral fragments and it dominates the coral deposits from 855 to 743 cm (Figs. 2B, 3B). Fe-Mn coated fragments of *D. pertusum* are found at 866–855 cm, whereas at 742–714 cm and at 706–699 cm this species co-occurs with *M. oculata* and *D. dianthus*.

Unit C (699–590 cm) – Unit C is dominated by coral rubble (CPP C4: 699–669 cm, CPP C5: 641–590 cm) and sediments with scattered corals (CPP D5: 669–641 cm). Between 699 and 598 cm, the coral

clasts are first composed of a mix of *D. pertusum*, *M. oculata* and *D. dianthus* (699–668 cm), then, set between two unconformities, by *M. oculata* and *D. pertusum* (668–636 cm), and finally by *D. pertusum* and *D. cornigera* (636–606 cm) (Fig. 2B).

Unit D (590–423 cm) – This unit is characterised by coral rubble (CPP C5: 590–561 cm, CPP C6: 553–423 cm). From 590 to 436 cm the coral deposits mainly consist of a mix of *D. pertusum*, *M. oculata* and *D. dianthus* (598–561 cm), followed by a section dominated by *D. pertusum* (553–436 cm; Fig. 2B). This change in species composition is marked by an unconformity in mound development (561–553 cm) dominated by iso-oriented bivalves and preceded by Fe-Mn coated corals (Figs. 2B, 3C). The uppermost section of this unit (436–423 cm) contains a mix of *D. pertusum*, *M. oculata* and *D. dianthus*.

Unit E (423–174 cm) – This unit starts with a gradual change from coral rubble (CPP C6: 423–413 cm) to slightly collapsed coral framework (CPP B2: 413–215 cm), followed by another gradual change to coral framework buried in living position (CPP A1: 215–174 cm). Unit E is preceded by the presence of a potential hiatus in coral mound formation and is entirely formed by a mix of *D. pertusum*, *M. oculata* and *D. dianthus* fragments (Figs. 2A).

Unit F (174–0 cm) – The coral deposits in this unit change from coral framework buried in living position (CPP A1: 174–153 cm) to sediments with scattered coral fragments (CPP D6: 153–87 cm), followed by slightly collapsed coral framework (CPP B3: 77–0 cm). From 174 to 24 cm, the coral facies consist of *D. pertusum*, while in the uppermost 24 cm the taxonomic composition drastically changes to a mix of *M. oculata* and *D. pertusum* (Fig. 2A).

4.1.2. Mound development

The age model of core MD13-3469G is based on 59 coral samples that were dated by means of U-Th series and whose age ranges from 589^{+248}_{-199} ka BP to 9.30±0.09 ka BP (Fig. 4, Tables S3, S4), indicating that periodic coral growth at this location began during/before ~Marine Isotopic Stage 11 (MIS 11) and ceased during the Early Holocene 9.30 ka BP. From these samples, 47 (80 %) correspond to deglacials and temperate interstadials (i.e. MIS 9c, 7a and 5c) identified as 3.5–4.1 δ^{18}O‰ in the Lisiecki and Raymo δ^{18}O stack (Lisiecki and Raymo, 2005), 9 (15%) to glacial periods (i.e. MIS 10 and MIS 6; Fig. 4A) and 3 of them do not fit in either, due to the large age uncertainty associated to the samples. Due to the considerable error associated with MIS 10 coral ages, their glacial age must therefore be treated with caution.
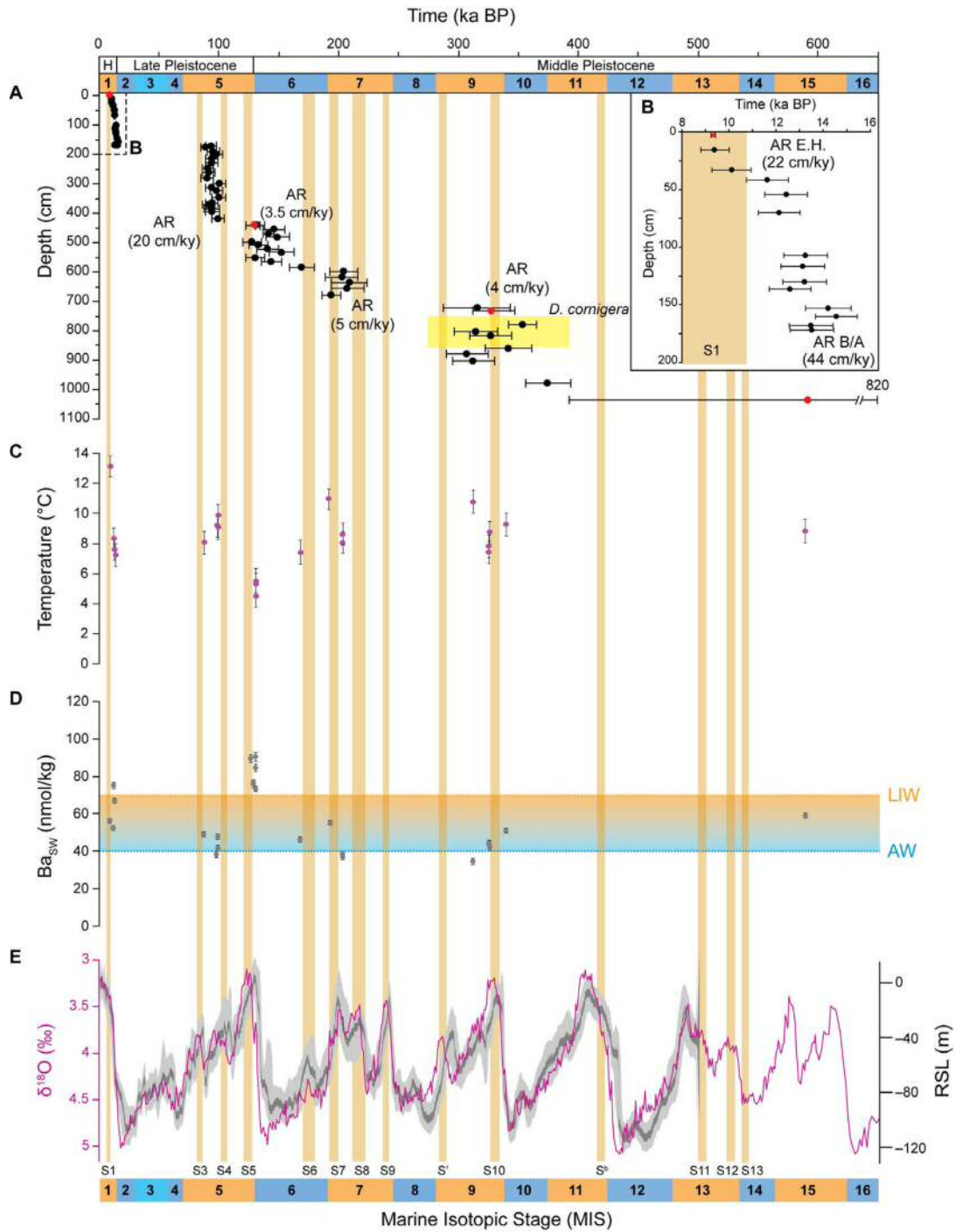
Figure 4. (A) MD13-3469G U-Th coral ages (black dots: laser ablation, red dots: solution) with associated 2σ uncertainties against core depth and aggradation rates (ARs) of each mound formation phase. The brown bars indicate sapropel events S1–S13 (Ziegler et al., 2010; Konijnendijk et al. 2014); the yellow rectangle indicates a mound evolution phase dominated by *D. cornigera* assemblages. (B) coral mound evolution during the Bølling-Allerød and Holocene, with coral ages against core depth and the ARs of the two mound formation phases. (C) Li/Mg derived Sea Water Temperatures (SWTs), (D) Ba/Ca derived Ba$_{SW}$ values and (E) LR04 δ^{18}O (‰) stack data for the last 650 ka (Lisiecki and Raymo, 2005) and Relative Sea-level dataset from Grant et al. (2014). The orange and blue shading indicates odd and even numbered Marine Isotopic Stages (MIS). The green and blue dotted lines indicate the present-day Ba$_{SW}$ values of Atlantic (AW) and Levantine Intermediate (LIW) water masses (Jacquet et al. 2016; Roy-Barman et al., 2019).

The age model hints towards the presence of five mound formation periods, covering time intervals between ~5 and ~46 ka, can be identified (Fig. 4A). Four mound stagnation periods are also observed, with durations ranging from ~24 to ~98 kyr (Fig. 4A). The first mound formation period, corresponding to Unit B, extends from ~346 to ~305 ka BP, with an AR of 4 cm kyr^{-1} and predominantly matches with the MIS 9 (Fig. 4A). However, it must be considered that an age inversion affects one of the samples within this period. This is followed by a potential mound formation hiatus that lasts for ~98 kyr and is coincident with the MIS 8 glacial and the start of MIS 7 (Fig. 4A). During MIS 7a-c interglacial, another short mound growth period occurred, going from ~207 to ~192 ka BP and corresponding to Unit C. This mound formation phase is characterised by an AR of 5 cm kyr^{-1} (Fig. 4A). Between this mound formation period and the following one, a short potential hiatus of ~24 kyr occurs, corresponding to the start of MIS 6 glacial in Lisiecki and Raymo (2005; Fig. 4A). The mound development period equivalent to Unit D, takes place during MIS 6 glacial and the deglacial prior to MIS 5. This period goes from ~168 to 127 ka BP and corresponds to the lowest ARs observed in this study (3.5 cm kyr^{-1}). Within CPP C6 and between 426 and 419 cm core depth, a drastic decrease in coral content (vol.%) and the significantly different coral ages indicate the presence of a potential hiatus in coral mound formation of ~29 ka (Figs. 2A, 4A). The following growth stage, which corresponds with Unit E, extends from 99 to 87 ka BP and is characterised by an AR of 20 cm kyr^{-1}. After this faster mound aggradation phase a long hiatus (i.e. 87 kyr) occurs, encompassing the majority of the last glacial period (MIS 2–4). In Unit F coral mound development starts again at 14.5 ka BP, soon after the onset of the B/A interstadial (14.7–12.7 ka BP), and lasts until 13 ka BP, when the mound enters in a short stagnation stage coincident with the Younger Dryas (YD; 12.8–11.8 ka BP; Fig. 4B). This mound formation period displays the highest AR of the whole core with a value of 44 cm kyr^{-1}. After the end of the YD, and corresponding with the start of the Early Holocene, the last mound growth period occurs in core MD13-3469G (i.e. 12.06–9.3 ka BP). This phase exhibits an AR of 22 cm kyr^{-1} and ends soon after the onset of the Sapropel event 1, when the mound enters in a stagnation stage and does not grow anymore until the present day (Fig. 4B).

4.1.3. Paleo-environmental proxies

From the 24 temperature values obtained, two were discarded because they showed negative values, which have most probably been caused by a diagenetic alteration of the samples (Table A5). The sample occurring at 129 ka BP also records an unexpected seawater temperature (1.0°C) that is unrealistic for such a shallow depth in any location outside of the polar regions, and below the known range tolerated by CWCs (Table A5). Therefore, this sample was not considered when interpreting the results. The remaining Li/Mg ratios for core MD13-3469G range between 2.9 and 4.3 µmol mol^{-1}, equating to SWTs between 4.6±0.7 and 13.1±0.7°C (Fig. 4C, Table A5). These SWTs reflect the variability following glacial and interglacial cycles. Nonetheless, mound growth in this sector of the CMP generally occurs when the SWTs are between 7 and 10°C (Fig. 4A–C). The highest SWT value (i.e. 13.1±0.7°C)

550 coincides with the youngest age of this core (9.3 ka BP), when the mound stopped growing (Fig. 4B,
551 C).
552
553 Coral Ba/Ca values acquired cover a range of 7.7–16.9 μmol mol^{-1} corresponding to a range of Ba$_{SW}$
554 from 34.7±1.7 to 89.4±2.2 nmol kg^{-1} (Fig. 4D, Table A5). From these samples, the majority range
555 between the two present day end-members, AW and LIW (Fig. 4D), and 29% is recording higher Ba$_{SW}$.
556 The highest Ba$_{SW}$ values occur around the onset of the last two deglacials. In contrast, the lowest values
557 occur within MIS 5, 7 and 9 interstadials (Fig. 4D).
558
4.2. Cabliers North (Core MD13-3470G)
559
560
561 *4.2.1. Visual and CT-based core description*
562
563 The core MD13-3470G, acquired from the northernmost end of the CMP, consists of 8.4 m of dense
564 CWC fragments (Fig. 5). Such fragments are embedded in an olive grey muddy sediment matrix, mixed
565 with sporadic remains of other invertebrates, such as gastropods, bivalves and echinoids. Visual
566 qualitative assessment indicated that 62% of the core's length is formed by coral deposits with very
567 abundant coral fragments (high coral abundance in Fig. 5), mostly located below 450 cm core depth
568 (Fig. 5B). In contrast, only 36% of the core's length corresponds to more dispersed but still abundant
569 coral fragments (medium coral abundance in Fig. 5) and 2% to sediments with scattered corals (low
570 coral abundance in Fig. 5).
571
572 CT scanning revealed that coral content in this core varies from 2.9 to 29.3 vol.% with an average value
573 of 14.7±4 vol.% (Fig. 5). This core displays a similar range of values to those of MD13-3469G, yet
574 coral vol.% values in MD13-3470G are less variable. When comparing visually characterised coral
575 fragment abundance and CT-derived coral vol.% in this core, there is not such an evident correlation as
576 in MD13-3469G. The combination of visual and CT-based analyses suggests that the predominant
577 species forming the coral deposits is the framework-building coral *D. pertusum*. This core only contains
578 two coral species that are abundant throughout its length: *D. pertusum* and *M. oculata* (Fig. 5). A gradual
579 change from *D. pertusum* to *M. oculata* dominated facies can be clearly observed towards the top of the
580 core (Figs. 3A, 5). The CT scan analyses also allowed to identify two CPPs: deposits containing coral
581 framework buried in living position (CPP A), which dominate in the lower part of the core, and slightly
582 collapsed coral framework (CPP B), defined by the same clast size and inclination values as in section
583 4.1.1, dominating the upper portion of the core. In contrast to MD13-3469G, no unconformities in coral
584 mound evolution are observed throughout this core.

585

586
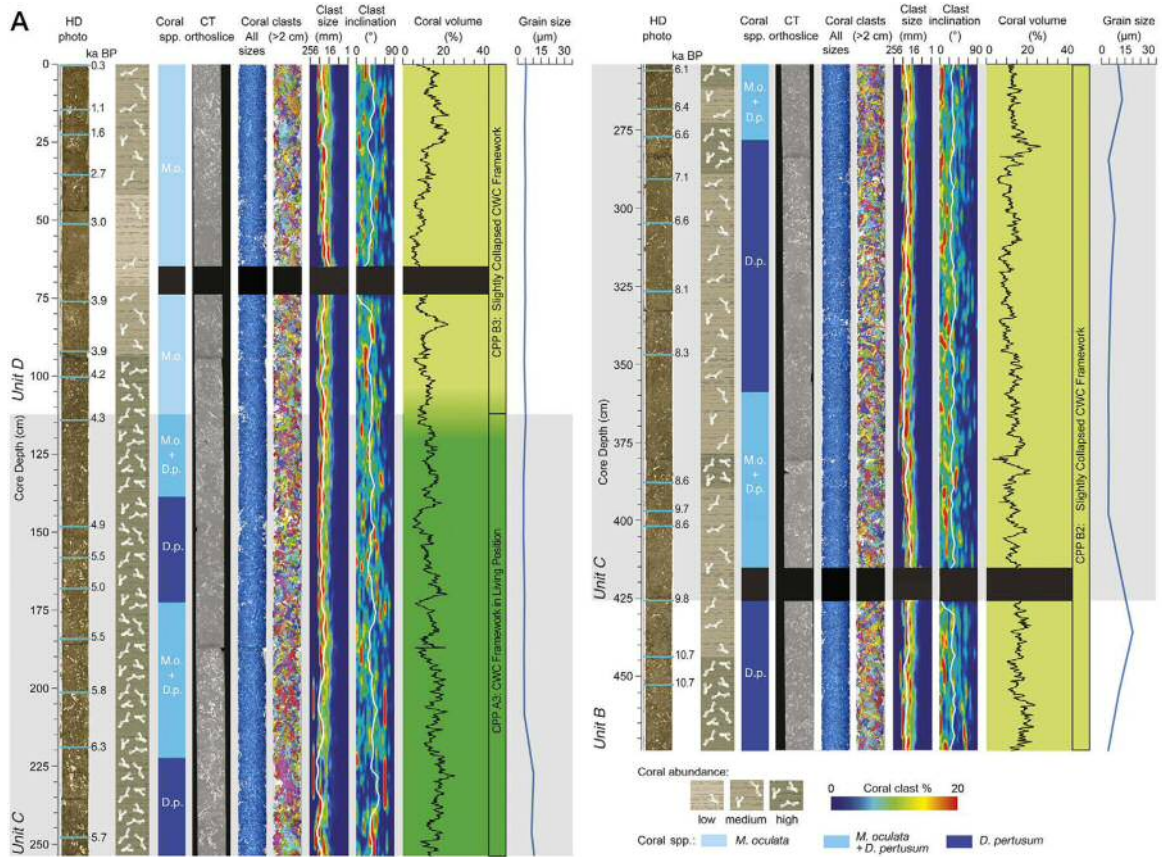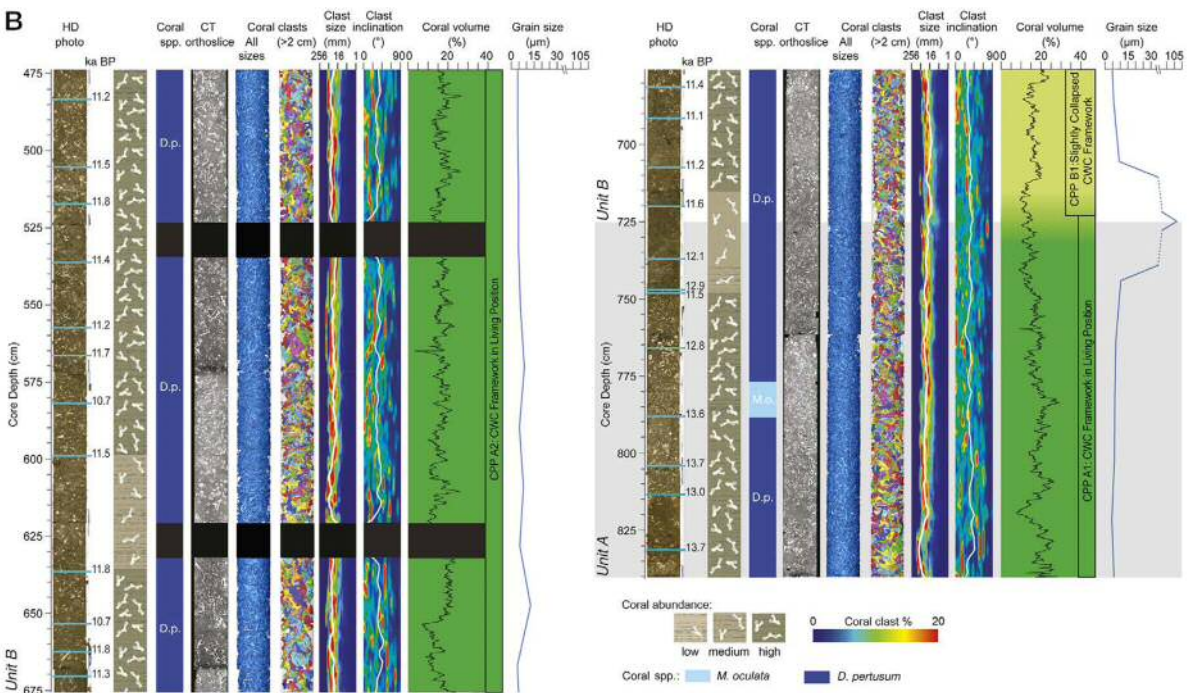
Figure 5. Log of the MD13-3470G core (A: 0–474 cm, B: 474–840 cm core depth). From left to right: core HD photo with location of the coral samples acquired for uranium series dating (blue lines) and the corresponding ages; stratigraphic representation of coral abundance; changes in the dominating species conforming the coral deposits; raw image of the core CT scans; 3D image of the CT scans including all segmented coral clasts; 3D image of the CT scan including coral clasts >2 cm; coral clast size distribution (white line: mean clast size); coral clast inclination (white line: mean clast inclination);

22

coral volume per slice (200 µm) overprinted on the coral preservation pattern (CPP A-dark green: coral frameworks buried in living position; CPP B-light green: slightly collapsed coral framework). This figure can be found in supplementary material as four high resolution panels.

Average sediment grain size along the core oscillates between 3.7 (i.e. clay) and 105 µm (i.e. very fine sand) and displays an average value of 8.8±14.9 µm (i.e. fine silt) (Fig. 5). Grain size values are relatively constant throughout the core with only two peaks of 105 µm and 20 µm (i.e. medium silt) occurring at 723 and 435 cm core depth respectively (Fig. 5).

As for MD13-3469G, MD13-3470G has been divided into 4 different units according to a combination of coral ages, mound aggradation rates and the main sedimentological features, facilitating the description of the change in coral species, CPPs and mound formation stages (Fig. 5):

Unit A (840–723 cm) – The coral deposits in this unit are characterised by the presence of coral frameworks buried in living position (CPP A1: 840–723 cm; Fig. 5B). The coral fragments in the lowermost part of the core (840–723 cm) consist predominantly of *D. pertusum*, except for a short section going from 788 to 776 cm, where *M. oculata* dominates (Fig. 5B).

Unit B (725–425 cm) – This unit mainly consists of coral framework buried in living position (CPP A2: 675–474 cm) bounded by shorter sections of slightly collapsed coral framework in the lowermost and uppermost parts of the unit (CPP B1:723–675 cm, CPP B2:474–254 cm; Fig. 5). Coral fragments in this unit are dominated by *D. pertusum* (Fig. 5).

Unit C (425–113 cm) – This unit is characterised by the presence of slightly collapsed coral framework at the base (CPP B2: 474–254 cm) and coral framework buried in living position at the top (CPP A3: 254–113 cm; Fig. 5A). Between 415 and 359 cm a mix of *D. pertusum* and *M. oculata* occurs (Fig. 5A). Between 359 and 113 cm core depth the coral facies are composed of *D. pertusum* (359–278 cm, 254–223 cm, 173–139 cm) and a mix between *D. pertusum* and *M. oculata* (278–254 cm, 223–173 cm, 139–113 cm).

Unit D (113–0 cm) – The uppermost section of the core (113–0 cm), displays coral facies completely dominated by *M. oculata* (Fig. 5A) in the form of slightly collapsed coral framework (CPP B3:113–0 cm; Fig. 5A).

4.2.2. Mound development

The age model of core MD13-3470G is based on 51 coral samples that were U-Th dated, with ages ranging from 14.4 to 0.3 ka BP (Fig. 6A). From these samples, 5 (1%) correspond to the B/A interstadial, 24 (47%) to the Early Holocene, 13 (26%) to the Mid Holocene and 8 (16%) to the Late Holocene (Fig. 6A). Although the U-Th dating shows that mound development in this core is almost continuous, four main periods with varying mound formation rates can be identified (Fig. 6A).
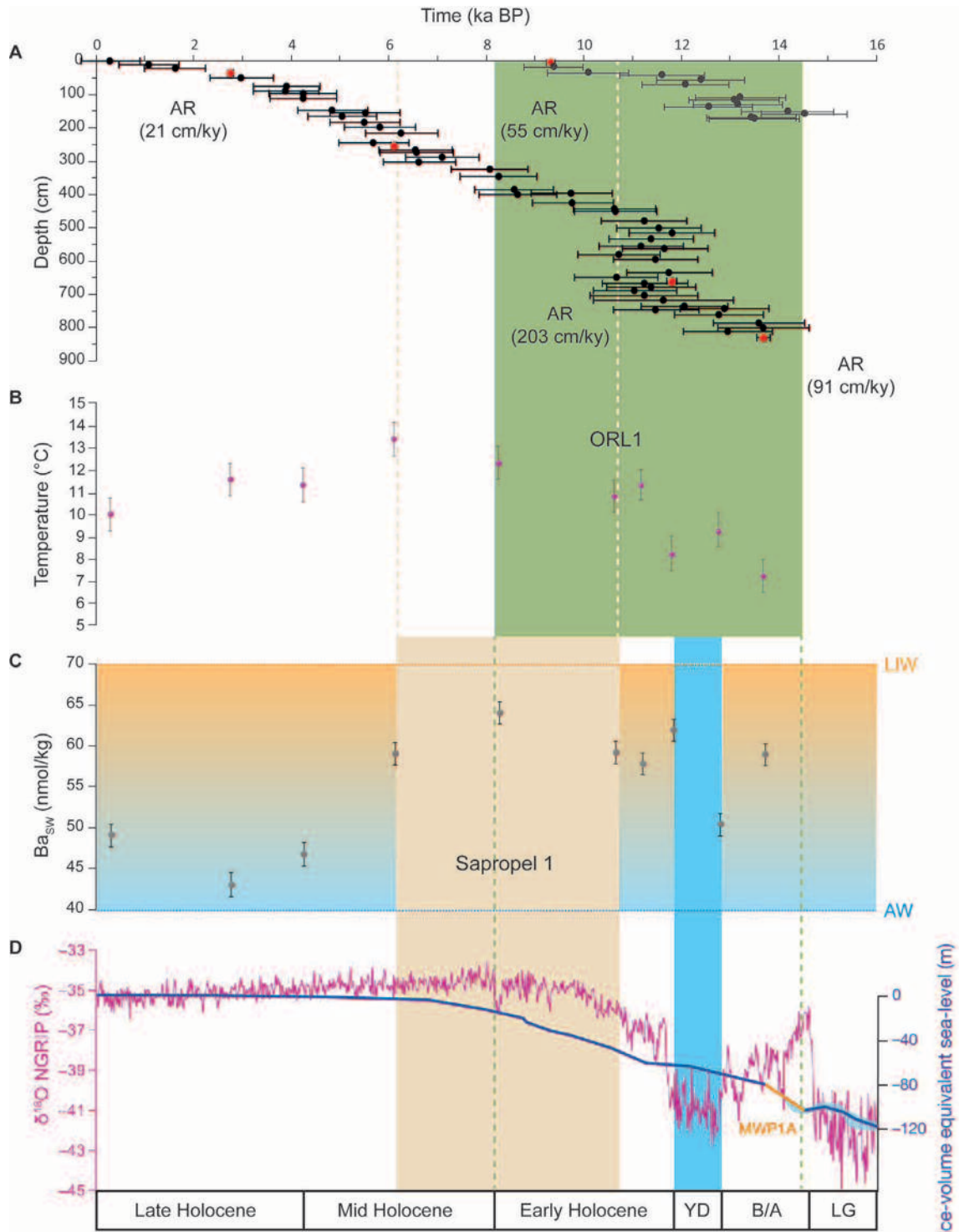
Figure 6. (A) MD13-3470G uranium series coral ages (black dots: laser ablation, red dots: solution) against core depth with aggradation rates (ARs) of each coral mound formation period. The blue bar indicates the duration of the Younger Dryas (YD) period; the brown and green rectangles indicate the dates of Sapropel event 1 (S1) and the Organic Rich Layer 1 (ORL1) in the Eastern and Western Mediterranean Sea respectively (Ziegler et al. 2010; Rohling et al., 2015). (B) Li/Mg derived Bottom Water Temperatures (BTWs), (C) Ba/Ca derived Ba_{SW} values and (D) NGRIP $\delta^{18}O$ (‰ SMOW) data for the last 16 ka (North Greenland Ice Core Project members, 2004) and ice-volume equivalent sea-level from Lambeck et al. (2014). B/A: Bølling Allerød; LG: Last Glacial. The green and blue dotted lines indicate the present-day Ba_{SW} values of Atlantic (AW) and Levantine Intermediate (LIW) water masses.

The first mound formation phase falls within the B/A interstadial and corresponds to Unit A. It extends from 13.69 to 12.8 ka BP and presents an AR of 91 cm kyr^{-1}. At 723 cm, coincident with the grainsize maxima and the change between CPP A1 and CPP B1, a short coral mound stagnation period synchronous with the YD, occurs (Figs. 5B, 6). With the onset of the Early Holocene, the fastest mound growth period observed in this study occurs (11.8–10.7 ka BP), with an AR of 203 cm kyr^{-1} and corresponding to Unit B (Figs. 5, 6A). During the rest of the Early Holocene and until the start of the Late Holocene, which coincides with Unit C, the coral mound keeps growing but at a slower pace (10.7–3.8 ka BP, AR = 55 cm kyr^{-1}). In the Late Holocene, from 3.8 to 0.29 ka BP and corresponding with Unit D, the AR of the mound is even slower (AR = 21 cm kyr^{-1}; Fig. 6A). This matches with a change in the coral species forming the CWC deposits, which start to be entirely dominated by *M. oculata*.

4.2.3. Paleo-environmental proxies

The Li/Mg ratios for the core MD13-3470G range between 2.8 and 3.8 µmol mol^{-1} and the corresponding SWTs show values between 7.2±0.7 and 13.4±0.8°C (Fig. 6B; Table A5). They exhibit a warming trend from the B/A interstadial until the Mid Holocene (6.1 ka BP), where the SWT reaches 13.4°C. After that age, SWTs start decreasing again until modern times (0.3 ka BP–10±0.7°C). The fastest mound growth in this core occurs when the SWTs are between 8 and 11°C (Fig. 6B), a potentially optimal temperature range similar to that observed in the southern CMP (i.e. core MD13-3469G).

Coral Ba/Ca values range from 9.1 to 12.5 µmol mol^{-1}, which results in a range of 43.1±1.4 to 63.6±1.3 nmol kg^{-1} Ba$_{SW}$ (Fig. 6C; Table A5). All the samples recorded Ba$_{SW}$ within the present range in the Mediterranean (Roy-Barman et al., 2019). Two of the highest Ba$_{SW}$ values correspond with the B/A interstadial (13.69 ka BP) and the end of the YD (11.8 ka BP). Another Ba$_{SW}$ maximum takes place in the transition from the Early Holocene to the Mid Holocene (8.3 ka BP), from which the values show a decreasing trend towards the present (Fig. 6C). Finally, the highest ARs observed in this core occur when Ba$_{SW}$ values range between ~58 and 62 nmol kg^{-1}.

5. DISCUSSION

Although the present-day distribution of living scleractinian CWCs in the Mediterranean Sea is mainly confined to submarine canyons and cliffs (Orejas et al., 2009; Fabri et al., 2017; Taviani et al., 2017; Titschack, 2019), the occurrence of multiple coral mound structures in the Alboran Sea and, to a minor extent, in the central Mediterranean suggests that there have been periods in the past when favourable environmental conditions supported the long-term formation of CWC reefs (Remia and Taviani, 2005; Martorelli et al., 2011; Fink et al., 2013; Lo Iacono et al., 2014, 2016; Corbera et al., 2019). Nonetheless, not much is known about the evolution of these geological features during the Pleistocene. For instance, even though most of the Alboran Sea coral mounds are considerably tall (i.e. >70 m in height), so far only the uppermost and thus the most recent development of the mounds has been described (Fink et

al., 2013, 2015; Stalder et al., 2018; Wang et al., 2019). Particularly, the WMM and EMM have been studied intensively, with ~80 coral ages from ~7 mounds presented so far (Fink et al., 2013, 2015; Titschack et al., 2016; Wang et al., 2019; Wienberg, 2019). However, due to the lack of cores encompassing longer periods, most of the research has focussed on the coral mound development since the Last Glacial Maximum (LGM) (Fink et al., 2013; Stalder et al., 2018; Wang et al., 2019). In this study we are able to expand that time frame by >390 ka, bringing unprecedented insights into the evolution of cold-water coral mounds in the Alboran Sea.

One of the main findings of this study is the large age difference in mound formation intervals between the south and north CMP cores (i.e. MD13-3469G and MD13-3470G), with the former encompassing from >390 until 9.3 ka BP and the latter from 14.4 to 0.3 ka BP (Figs. 4A, 6A). Furthermore, the cores present overlapping mound growth periods from the B/A until the Early Holocene, allowing for a continuous tracking of CMP evolution since the middle Pleistocene. Considering that the gravity cores retrieved 10.4 and 8.4 m of coral-bearing sediments in areas where the coral mounds were up to 50–60 m in height, only the most recent developmental stages of the mound could be elucidated in this study. The modern age of the uppermost corals dated in the northern CMP and the concurrent stagnation of its southern counterpart reflect the current state of the habitats observed on the coral mounds summit, which display living CWCs reefs on the northernmost sector and dead CWC frameworks on the southernmost mound (Corbera et al., 2019).

5.1. Coral mound development during the Middle and Late Pleistocene

Throughout the Middle and Late Pleistocene (773–14.7 ka BP; Core MD13-3469G Units A, B, C, D, E), mound growth periods in the CMP generally occurred during temperate interstadials (i.e. MIS 9c, 7a and 5c), but with quite low ARs (4–23 cm ka^{-1}; Fig. 4A). No mound formation is observed during glacial periods, with the exception of MIS 6 glacial, which presents the lowest ARs observed in this study (3.5 cm ka^{-1}; Fig. 4A). The absence of growth during MIS 8 and MIS 2–4 glacials is represented in the core record as hiatuses in coral mound development, that lasted up to ~98 ka.

During the Middle Pleistocene (773–126 ka BP; Core MD13-3469G Units A, B, C, D), the first coral ages (Unit A-B: 588–373 ka BP) and the CPPs in which they are found, suggest an extremely slow mound formation stage and could be the result of either particularly limited coral growth and/or erosional processes that altered part of the mound development stratigraphic record. This would match with what has been observed in the CT-scans, which display sediments with mostly unidentifiable scattered bioclasts, coral rubble deposits (CPP D1, C1) and an unconformity (Fig. 2B).

The following mound growth stage (Unit B: 352–306 ka BP; Fig. 4A) started after a period of stagnation corresponding to MIS 10 glacial and displays an average AR of 4 cm ka^{-1}. The older and less preserved coral deposits of this mound development period (CPP D2, D3, D4 and CPP C2, C3), which are

26

separated by unconformities, indicate an intermittent mound formation stage marked by a gradual change in the taxonomic composition of the coral clasts, from facies formed by *D. pertusum*, *M. oculata* and *D. dianthus* to a *D. cornigera* dominated one (Figs. 2B, 3B). Although no relevant changes in terms of SWTs or Ba/Ca are observed during this period, the change in the dominating species could be related to the presence of unfavourable environmental conditions for the growth of *D. pertusum* and *M. oculata* during MIS 9. Dendrophyllid corals are known to withstand a wider range of environmental conditions, including higher temperatures and turbidity values (Naumann et al., 2013; Gori et al., 2014, 2015; Castellan et al., 2019). Furthermore, these corals used to dominate the Mediterranean coral communities before the Plio-Pleistocene transition, when less marked glacial-interglacial cycles occurred and the temperatures were higher (Vertino et al., 2019). Currently, dendrophyllid corals form assemblages in the warm and oligotrophic Eastern Mediterranean Basin (Orejas et al., 2019 and references therein), where the high temperature and salinity values of Levantine waters (i.e. 13.9–17.3ºC and 38.8–39.1) prevent *D. pertusum* and *M. oculata* from proliferating. It is important to remark that the presence of a mound formation unit dominated by dendrophyllids has never been observed before on a submerged coral mound. However, the available data is not enough to completely describe the environmental setting in which this 110 cm long section formed. In the younger period of this mound formation stage (741–680 cm core depth), the species composition changes back to a *D. pertusum* dominated facies, which represents the main constituent of the Cabliers coral framework. This remains generally constant for the rest of the mound's evolution, although variations are observed in the accompanying taxa (e.g. *M. oculata* and *D. dianthus*; Fig. 2). This mound formation phase is followed by a coral mound stagnation period of ~98 ka that encompasses the MIS 9a-b, MIS 8 and MIS 7d-e (Figs. 2B, 4A).

The absence of coral growth throughout MIS 7d stadial (Fig. 4A) might be related to a drastic sea-level and temperature decrease, that could have promoted variations in the surface circulation of the Alboran Sea (Vargas-Yáñez et al., 2002; Lo Iacono et al., 2014), probably affecting upwelling processes and thus primary productivity. Towards the second half of MIS 7, when the temperatures and sea-level rose again, coral mound formation occurred (Unit C: 207–192 ka BP). Yet, it was characterised by the presence of scattered corals fragments within the matrix sediments (CPP D5), coral rubble deposits (CPP C5) and two unconformities, which indicates this was not a thriving mound formation period, as confirmed by its low AR of 5 cm ka^{-1} (Figs. 2B, 4A).

After a short stagnation stage of ~24 ka matching with the start of MIS 6 glacial, the last mound growth period of the Middle Pleistocene started (Unit D: 168–127 ka BP; Fig. 4A). However most of the ages cluster towards the end of the MIS 6, between 150-127 ka BP. The low SWTs observed during this period (<6.5°C; Fig. 4C) confirm these samples grew during a cold interval. Although observing coral growth in a glacial setting does not fit with the general pattern of this mound's development, coral deposits corresponding to this period are only formed by *D. pertusum* (Fig. 2), demonstrating the higher capability of this species to cope with temperatures <7°C (Nauman et al., 2014). In addition, the

presence of coral rubble (CPP C5), Fe-Mn coated corals and one unconformity suggests that the southern CMP mound did not develop under flourishing conditions during MIS 6 (Fig. 2B). Instead, the low AR (3.5 cm ka^{-1}) indicates sporadic coral growth events, but without enough reef growth to promote significant mound formation. The unconformity observed during this period (561–551 cm, 143–129 ka BP; Figs. 2B, 3C) is defined by the occurrence of abundant and closely-packed parallel bivalve shells, some of them still displaying both of the valves, which indicates an in-situ ecological aggregation undergoing limited transport by moderate bottom currents (Kidwell and Holland, 1991; Hauser et al., 2008). The presence of thriving bivalve populations within CWC reefs has been described in many Atlantic coral mound provinces, which display, among other species, abundant individuals of the genus *Acesta* (Hovland & Mortensen 1999; Buhl Mortensen et al., 2016). The unidentified bivalve facies observed here is placed between coral ages ranging from 143 to 129 ka BP, thus indicating that it could correspond to an interval of cold conditions related to the end of MIS 6. Bivalve assemblages are known to thrive in the Mediterranean during glacial periods (Colantoni, 1973; Taviani and Colantoni, 1979; Bouchet and Taviani 1992; López-Correa et al., 2006), thus they might have replaced coral assemblages during this colder phase of MIS 6.

During the Late Pleistocene (126–14.7 ka BP), coral mound growth only occurred during MIS 5c (Unit E: 99–87 ka BP) and it was preceded by a 29 kyr long mound stagnation period (Fig. 4A). Excluding MIS 5e, when the sea-level was significantly higher, the absence of corals during the rest of MIS 5 cannot be attributed to this factor. The only exception would occur during MIS 5a, as some evidences in the Mediterranean Sea indicate the presence of a sea-level highstand characterised by rapid changes, which raised 1 m above the current sea-level (Dorale et al., 2010). Throughout MIS 5b-d, other environmental variables (e.g. primary productivity, dissolved oxygen, water mass circulation) might have played a relevant role limiting coral mound formation. The mound formation phase that occurred during MIS 5c is characterised by the presence of slightly collapsed coral framework deposits (CPP B2), followed by coral framework in living position (CPP A1), and corresponds with higher ARs (25 cm ka^{-1}) than those observed during the Middle Pleistocene (<5 cm ka^{-1}). The SWTs and the Ba$_{SW}$ values registered by corals during this time span do not show significant differences from those observed in previous mound formation phases (Fig. 4C, D), which means that other environmental variables might have had a greater effect on promoting a higher pace of mound growth. One of them could be food supply related to surface productivity, which has previously been regarded as a key variable affecting the development of several coral mounds, including the WMM and EMM provinces, located a few kilometres south of the CMP (Fink et al., 2013; Wang et al., 2019).

5.2. Coral mound development from the Bølling-Allerød to the present-day

Both MD13-3469G (Unit F) and MD13-3470G (Unit A, B) cores, collected respectively from the southern and northern sectors of the CMP, exhibit pronounced coral mound formation during the B/A interstadial and the Early Holocene (Figs. 4B, 6A), as observed in the Melilla Coral Provinces (Fink et

al., 2013; Wang et al., 2019). Mound formation started just after the Melt Water Pulse-1A (MWP-1A), which supposed a sea-level increase of 20 m in ~500 years. With the continuous sea-level increase, growth on the southern mound stopped at 9.3 ka BP, while the shallower mound located at the northernmost region of the CMP is still growing in the present day (Corbera et al., 2019). Similar to what has been observed in the Pleistocene and given the uncertainty of the U-Th solution ages, if we assume a continuous stratigraphic record, our data suggests that mound formation did not occur during the cold stadial interval of the Younger Dryas (YD; 12.8–11.8 ka BP). This fits again with what has been observed in other Alboran Sea coral mounds (Fink et al., 2015; Wang et al., 2019). In Fink et al. (2015) the authors speculate that the absence of coral growth during the YD could be the result of a change in the Alboran Sea water mass circulation, affecting the stability of the WAG and EAG, thus limiting the formation of upwelling regions and ultimately surface productivity. Nonetheless, the Ba/Al increase observed in sediment cores from other studies point to an enhanced productivity during this period (Jiménez-Espejo et al., 2015; Martinez-Ruiz et al., 2015), which is also reported in the diatom record from the Alboran Sea (Barcena et al., 2001). Jiménez-Espejo et al. (2015) and Martinez-Ruiz et al. (2015) also reported lower oxygenation throughout the YD, a factor that might have also affected coral growth during this cold period. The absence of growth during the YD also matches with a drastic grain size increase registered in core MD13-3470G (i.e. from fine silt to very fine sand; Fig. 5B). Fink et al. (2013) and Wang et al. (2019), also described increased sediment grain size related to intense hydrodynamic conditions during this cold stadial, yet with considerably lower values (~15–27 μm) than the ones observed in the northern CMP (105 μm). Although we measured total sediment instead of just measuring the siliciclastic fraction, the temporal correspondence of the grain size peak observed in this study with the one observed in Fink et al. (2013) and Wang et al. (2019) suggests that it could be related to an overall intensification of the currents associated to the upper layer of the LIW.

Following the YD period, mound development restarted simultaneously in both CMP regions with the onset of the Early Holocene. At the southern sector, this last mound formation period (i.e. Unit F: 12.1– 9.3 ka BP) exhibited an AR of 24 cm ka^{-1}, which occurred before the mound entered in a stagnation stage until the present day (Fig. 4B). This AR value is considerably lower than the rates observed at the WMM (75–107 cm ka^{-1}) and EMM (140–291 cm ka^{-1}) during the Early Holocene (Fink et al., 2013; Stalder et al., 2015; Wang et al., 2019). Yet, the low AR during the most recent development of the southern CMP matches with the prevalence of *M. oculata* over *D. pertusum* in the coral deposits, which presumably has a lower capability to form mounds due to it thinly branched and more fragile skeleton (Fig. 2A; Wienberg et al., 2019). During the same period, the northernmost region of the CMP presents a flourishing growth phase from the onset of the Early Holocene (i.e. 11.8 ka BP) until 10.7 ka BP (Unit B), with an AR of 203 cm ka^{-1} and a 280 cm thick coral deposit, formed by *D. pertusum* framework preserved in living position (CPP A2; Figs. 5, 6A). This high AR is within the values observed in the EMM and is comparable to the rates observed in the thriving Northeast Atlantic mounds (Titschack et al., 2015).

835 After 10.7 ka BP the coral deposits in the northern CMP mound gradually changed from *D. pertusum*
836 to *M. oculata* dominated facies, which also translated into a continuous decrease of the ARs until the
837 present-day (Figs. 5A, 6A). From 10.7 to 3.9 ka BP (Unit C-D) the AR decreased to 56 cm ka^{-1}, which
838 is within the range of ARs observed on the WMM during this period (12–107 cm ka^{-1}) (Wang et al.,
839 2019). Furthermore, whereas no mound growth is observed on the WMM or EMM from 3.8 ka BP to
840 the present-day, the northern region of the CMP continued to develop at a very slow pace (Unit D: 22
841 cm ka^{-1}), almost exclusively sustained by the growth of *M. oculata*. Such change in species composition
842 throughout the Holocene has been observed in other Alboran Sea coral mounds (Stalder et al., 2015;
843 Wienberg et al., 2019) and is apparent in the current living CWC assemblages found in the
844 Mediterranean Sea, which are dominated by *M. oculata* interspersed with some colonies of *D. pertusum*
845 (Orejas et al., 2009; Taviani et al., 2017; Corbera et al., 2019). It is hard to exactly determine the
846 environmental trigger of this change in species dominance throughout the Holocene, yet it is likely that
847 rising SWTs towards the Mid Holocene combined with lower food supply, coinciding with the end of
848 Organic Rich Layer 1 (ORL1; western Mediterranean equivalent of sapropels), might have had
849 detrimental effects for the proliferation of *D. pertusum* (Martrat et al., 2004; Fink et al., 2013; Wang et
850 al., 2019). In contrast, *M. oculata*, which is known to withstand higher temperatures and unstable
851 conditions (Naumann et al., 2014), might have been able to cope with these drastic environmental
852 changes.

854 Besides coral growth, persistent sediment sources are needed for coral mound development, since it
855 stabilises the coral framework, preventing it from collapsing and thus promoting a fast mound formation
856 (Wienberg and Titschack, 2017). Hence, besides the lower capability of *M. oculata* to form mounds
857 (Wienberg et al., 2019), the decreased ARs observed during the Mid and Late Holocene could also be
858 caused by a decreased sediment supply after the end of the sea-level rise (Church et al., 2008; Vacchi
859 et al., 2016). This hypothesis is consistent with decreasing regional Ba$_{SW}$ values at our site since the end
860 of the last deglaciation (Fig. 6C), a pattern that might have been driven by either a reduction of riverine
861 run-off in the Alboran Sea or by a reduced amount of suspended particles being transported by
862 intermediate waters.

864 While the Pleistocene stages of any Mediterranean coral mound have not been described so far, the
865 development of the CMP during deglacials and temperate interstadials seems to occur before that of the
866 Irish and Norwegian coral mounds. The latter solely develop during interglacials (Roberts et al., 2006;
867 Kano et al., 2007; Frank et al., 2011; de Haas et al., 2009; Thierens et al., 2010), when the ice-sheets
868 retreat and the polar front moves northwards, enhancing the flow of cold nutrient-rich waters onto the
869 continental shelves (Frank et al., 2011; Titschack et al., 2015). In contrast, the coral mounds of the
870 adjacent Gulf of Cadiz, the closest mound region to the Alboran Sea, show an opposite evolution pattern
871 during the Pleistocene, with mound growth occurring almost exclusively during glacial periods
872 (Wienberg et al., 2010; Vandorpe et al., 2017). This is due to the oceanographic configuration of the

873   Gulf of Cadiz, which promotes enhanced surface productivity during glacial periods owed to a

874   strengthened upwelling along the Azores front and intensified eolian dust transport, providing a

875   sufficient food supply for the development of the mounds (Bertrand et al., 1996; Volkov and Fu, 2010;

876   Wienberg et al., 2010).

877

878   On the other hand, the contrasting mound formation rates observed during the Holocene and the present-

879   day differences in living coral abundance between northern and southern CMP (Corbera et al., 2019)

880   suggest that the latter has generally been exposed to less suitable environmental conditions for coral

881   mound formation. This also applies when comparing the southern CMP mound development (417 m

882   water depth) to that of the WMM and EMM (251–379 m water depth; Fink et al., 2013; Stalder et al.,

883   2015; Wang et al., 2019). The distinct paleo-evolution of the mounds within the CMP and the fact that

884   its northernmost mound still manages to thrive while all coral mounds in the Alboran Sea are in a stage

885   of decline, reflects the paramount role of this coral mound province within the Mediterranean Basin.

886

887   5.3. Local environmental variables and regional paleo-climatic events controlling the
888   development of the Cabliers mounds

889

890   The fastest aggradation rates of the CMP occurred during periods when the SWTs ranged between ~7–

891   11°C (Figs. 4, 6), fitting within the known temperature range tolerated by *D. pertusum* and *M. oculata*

892   (4–13°C; Roberts et al., 2006). Ba/Ca values observed in this study (7.7–16.9 µmols mol^{-1}; Table A5)

893   match with the ones observed in Norwegian coral mounds, generally ranging between 8 and 20 µmols

894   mol^{-1} (Raddatz et al., 2016). The high Ba_{SW} values associated to mound growth during deglacials (>70

895   nmol kg^{-1}; Fig. 4D) could be explained by a combination of increased LIW influence at the site and

896   enhanced riverine input derived from the Atlas glaciers melting into the Moulouya river (Hughes et al.,

897   2011). The latter ends directly south of the CMP, most probably increasing particulate and thus

898   dissolved Ba in the region. This would match with what has been observed in previous studies, where

899   increased Ba_{SW} has been suspected to be associated with enhanced riverine input (Raddatz et al., 2016).

900   On the other hand, Ba_{SW} observed during mound formation occurring in temperate interstadials (~35–

901   55 nmol kg^{-1}; Fig. 4D) correspond with present-day values closer to those of the AW (Jacquet et al.,

902   2016; Jullion et al., 2017; Roy-Barman et al., 2019). Despite the mound's summit is too deep to be

903   bathed by the former water mass vertical mixing processes, such as downwelling and/or internal waves

904   (Oguz et al., 2014; Van Haren et al., 2014), may have brought shallower waters down to the mound

905   during the examined interstadial periods, thus reducing the amount of Ba_{SW} around the growing corals.

906

907   The most pronounced mound formation stages of the CMP occurred during deglacials and temperate

908   interstadials, but not during glacials (Figs. 4, 6). During warm periods, a larger amount of Atlantic

909   Water flows into the Mediterranean basin through the Strait of Gibraltar due to high sea-levels (Sierro

910   et al., 2005). The higher inflow of AW together with enhanced freshwater input derived from

911   continental melt-waters causes a reduction of the surface water salinity, thus promoting stratification of

the water column and a far less evident formation of West Mediterranean Deep Water (WMDW) in the Gulf of Lion (Rogerson et al., 2008; Toucanne et al., 2012). This leads to a slowdown of the Mediterranean thermohaline circulation (Rogerson et al., 2008; Toucanne et al., 2012; Stumpf et al., 2010) and a simultaneous reduction of LIW formation in the Eastern Mediterranean basin (Toucanne et al., 2012; Jiménez-Espejo et al., 2015). Nonetheless, the high values of our Ba_{sw} data towards the transition into warmer periods (Fig. 4D) is indicative of an increased influence of the LIW at the coral site, most likely driven by the sea-level rise. These findings coincide with observations of Taviani et al. (2017), who suggested an evident positive impact of the LIW on Mediterranean CWC communities, since currently all thriving CWC assemblages are found within the depths bathed by this water mass (Orejas et al., 2009; Fabri et al., 2017; Taviani et al., 2017; Corbera et al., 2019; Lo Iacono et al., 2019). Furthermore, the structure of the water column in the Alboran Sea displays a water mass interface between AW and LIW at an average depth of 200 m. Water mass interfaces are known to accumulate particulate matter, mainly consisting of plankton (Mc Manus et al., 2003; Mienis et al., 2007). The interaction between two water masses might promote the creation of internal waves, which propagate along the interface, increasing sediment resuspension and vertical mixing, which could promote increased transfer of organic matter to deeper regions (Davies et al., 2009; White and Dorschel, 2010; Van Haren, 2014). Internal waves have been observed in the Alboran Sea at 250 m water depth with an amplitude of up to 90 m, reaching down to 300 m water depth (Van Haren, 2014). During deglacials and temperate interstadials the AW-LIW interface was closer to the southern CMP mound summit, which combined with the potential presence of internal waves might have contributed to provide enough food supply to promote mound formation.

Although LIW influence on the mounds increases during warm periods, Toucanne et al. (2012) reported that its flow intensity fluctuates following Milankovitch cycles. During insolation maxima, North African monsoons migrate northwards, which results in higher precipitation over the Nile watershed and the North African fossil drainage system (Rohling et al., 2002, 2004; Osborne et al., 2010). This causes an increase in nutrient-rich freshwater inflow, particularly to the Eastern Mediterranean Basin, that promotes a strong stratification of the water column, enhanced primary productivity and reduced deep-water ventilation, which in turn trigger the deposition of sapropels (i.e. bands of organic-rich sediments; Capotondi et al., 2011; Grant et al., 2016; Wu et al., 2018). The water column stratification in the Eastern Mediterranean basin caused during sapropel events triggers a collapse in the LIW's formation (Filippidi et al., 2016), which translates into a reduced circulation of this water mass in the West Mediterranean Basin and ultimately in the Strait of Gibraltar (Toucanne et al 2012; Bahr et al., 2015). Additionally, the water mass bathing the mounds would present lower oxygen levels due to the reduced ventilation characteristic of sapropel events in the Eastern Mediterranean Basin (Grant et al., 2016), and this could have had detrimental effects for coral growth. Indeed, these events are remarkably concurrent with periods of coral demise in the CMP, at least since the age of Sapropel 7 (S7; Fig. 4A). The decreased flow of LIW in the Alboran Sea during sapropel depositions might have also altered

somehow the structure of the interface between Atlantic and Mediterranean water masses, affecting the accumulation of organic matter and thus the food delivery to the mounds. Sapropel deposition has already been reported to have detrimental effects on CWC growth in the Eastern Mediterranean (Fink et al., 2015; Taviani et al., 2019), but clear evidence here supports a negative impact of these paleo-climatic events on coral mound formation in the westernmost Mediterranean as well, thousands of km away from the main region where they occur. Nevertheless, to formulate robust hypotheses on the effects of cyclic regional climatic changes on the development of coral mounds in the Mediterranean Sea, more coral-bearing cores of Pleistocene age from different regions of the basin should be acquired.

The differences in mound formation patterns between the northern (313 m water depth) and the southern (417 m water depth) CMP during the Holocene might be related to the vertical distance of the mounds' summits to the AW-LIW interface. With the last sea-level rise, a shallower AW-LIW interface might have prevented the southern mound from receiving enough food supply for coral sustainment. The shoaling of the interface (currently at ~200 m), together with the onset of the S1 deposition, which supposed a decrease in LIW formation, might have contributed to the demise of the southern CMP at ~ 9.3 ka BP (Fig. 4B). In contrast, the northern CMP underwent a particularly flourishing period during the Early Holocene, after which it continued to grow until the present day, albeit at a slower pace (Fig. 6A). The combination of suitable environmental conditions making this region unique in the entire Mediterranean during the Early Holocene, most likely included appropriate depth of the AW-LIW interface caused by sea-level changes, intensified productivity throughout the ORL1 deposition and high sediment input during deglaciation (Cacho et al., 2002; Lo Iacono et al., 2014; Fink et al., 2013; Wang et al., 2019). Overall, the present-day local oceanographic conditions, involving the jet of highly productive Atlantic waters, the action of internal waves and the presence of a downwelling region directly above the CMP (Oguz et al., 2014; Van Haren, 2014), which might have been present since the end of the sea-level rise around 7 ka BP, have most likely been crucial to sustain the CWC communities of its northernmost sector, after the rest of the Alboran Sea coral mounds entered in a stage of stagnation (Fink et al., 2013; Stalder et al., 2015; Wang et al., 2019).

6. CONCLUSIONS

In this study, we acquired 110 U-Th coral ages encompassing a period from the Middle Pleistocene to the present-day, which contributed to describe the development of two coral mounds located on opposite ends of the Cabliers Coral Mound Province (CMP; Alboran Sea-Western Mediterranean) and to expand our knowledge of coral mound development in the Mediterranean Sea beyond 50 ka BP back to the Calabrian stage. We conclude that:

– The fastest mound growth of the CMP occurred during deglacials and temperate interstadials, when sea-level changes placed the AW-LIW interface close enough to the mound's summit, probably enhancing food supply to the corals.

- Our data support a detrimental influence of Sapropel derived events, such as an interruption in LIW formation, on coral mound development in the Western Mediterranean Sea.
- The change from *D. pertusum* to *M. oculata* dominated coral deposits during the Holocene seems to have occurred at increasing seawater temperatures, and preceding periods of decreased food supply caused by the sea-level rise that placed the AW-LIW interface further away from the mounds.
- The high ARs and present flourishing state of the northern CMP mound makes it the most thriving CWC mound currently known in the Mediterranean Sea.
- Overall, the lower ARs and higher number of hiatuses observed in the southern CMP indicate that this sector is subjected to less favourable environmental conditions for mound formation than its northernmost counterpart. This is probably caused by the greater distance of this mound's summit to the AW-LIW interface.
- Contrasting mound development patterns between north and south CMP yield important insights on how local changes in oceanographic conditions can have crucial implications on coral mound formation.

REFERENCES

Addamo, A.M., Vertino, A., Stolarski, J., García-Jiménez, R., Taviani, M., Machordom, A., 2016. Merging scleractinian genera: The overwhelming genetic similarity between solitary *Desmophyllum* and colonial *Lophelia*. BMC Evol. Biol. 16, 1–17. doi:10.1186/s12862-016-0654-8

Anagnostou, E., Sherrell, R.M., Gagnon, A., LaVigne, M., Field, M.P., McDonough, W.F., 2011. Seawater nutrient and carbonate ion concentrations recorded as P/Ca, Ba/Ca, and U/Ca in the deep-sea coral *Desmophyllum dianthus*. Geochim. Cosmochim. Acta 75, 2529–2543. doi:10.1016/j.gca.2011.02.019

Angeletti, L., Castellan, G., Montagna, P., Remia, A., Taviani, M., 2020. The "Corsica Channel Cold-Water Coral Province" (Mediterranean Sea). Front. Mar. Sci. 7, 661. doi:10.3389/fmars.2020.00661

Bárcena, M.A., Cacho, I., Abrantes, F., Sierro, F.J., Grimalt, J.O., Flores, J.A., 2001. Paleoproductivity variations related to climatic conditions in the Alboran Sea (western Mediterranean) during the last glacial-interglacial transition: The diatom record. Palaeogeogr. Palaeoclimatol. Palaeoecol. 167, 337–357. doi:10.1016/S0031-0182(00)00246-7

1029 Bahr, A., Kaboth, S., Jiménez-Espejo, F.J., Sierro, F.J., Voelker, A.H.L., Lourens, L., Röhl, U., Reichart, G.J., Escutia, C.,
1030   Hernández-Molina, F.J., Pross, J., Friedrich, O., 2015. Persistent monsoonal forcing of mediterranean outflow water
1031   dynamics during the late Pleistocene. Geology 43, 951–954. doi:10.1130/G37013.1

1032 Bertrand, P., Shimmield, G., Martinez, P., Grousset, F., Jorissen, F., Paterne, M., Pujol, C., Bouloubassi, I., Buat Menard, P.,
1033   Peypouquet, J.P., Beaufort, L., Sicre, M.A., Lallier-Verges, E., Foster, J.M., Ternois, Y., 1996. The glacial ocean
1034   productivity hypothesis: The importance of regional temporal and spatial studies. Mar. Geol. 130, 1–9.
1035   doi:10.1016/0025-3227(95)00166-2

1036 Bett, B.J., Billett, D.S.M., Masson, D.G., Tyler, P.A., 2001. RRS Discovery Cruise 248, 07 Jul-10 Aug 2000. A
1037   multidisciplinary study of the environment and ecology of deep-water coral ecosystems and associated seabed facies
1038   and features (The Darwin Mounds, Porcupine Bank and Porcupine Seabight). Southampton Oceanography Centre,
1039   Southampton.

1040 Bonneau, L., Colin, C., Pons-Branchu, E., Mienis, F., Tisnérat-Laborde, N., Blamart, D., Elliot, M., Collart, T., Frank, N.,
1041   Foliot, L., Douville, E., 2018. Imprint of Holocene Climate Variability on Cold-Water Coral Reef Growth at the SW
1042   Rockall Trough Margin, NE Atlantic. Geochem. Geophys. Geosyst. 19, 2437–2452. doi:10.1029/2018GC007502

1043 Bosc, E., Bricaud, A., Antoine, D., 2004. Seasonal and interannual variability in algal biomass and primary production in the
1044   Mediterranean Sea, as derived from 4 years of SeaWiFS observations. Global Biogeochem. Cycles 18, GB1005.
1045   doi:10.1029/2003gb002034

1046 Bouchet, P., Taviani, M., 1992. The Mediterranean deep-sea fauna: pseudopopulations of Atlantic species? Deep Sea Res.
1047   Part A, Oceanogr. Res. Pap. 39, 169–184. doi:10.1016/0198-0149(92)90103-Z

1048 Buhl-Mortensen, P., Buhl-Mortensen, L., Purser, A., 2016. Trophic Ecology and Habitat Provision in Cold-Water Coral
1049   Ecosystems, in: Marine Animal Forests. Springer International Publishing, pp. 919–944. doi:10.1007/978-3-319-
1050   17001-5_20-1

1051 Cacho, I., Grimalt, J.O., Canals, M., 2002. Response of the Western Mediterranean Sea to rapid climatic variability during
1052   the last 50,000 years: A molecular biomarker approach. J. Mar. Syst. 33–34, 253–272. doi:10.1016/S0924-
1053   7963(02)00061-1

1054 Capotondi, L., Vigliotti, L., Bergami, C., Sangiorgi, F., 2011. The Dark Side of the Mediterranean Geological Record: the
1055   sapropel layers and a case study from the Ionian Sea, in: Marine Research at CNR. Dipartimento Terra e Ambiente—
1056   CNR, Roma, pp. 658–669.

1057 Carcassi, A., 1983. Ulteriore ritrovamento di *Acesta excavata* vivente in Mediterraneo. Boll. Malacol. 19, 264.

1058 Case, D.H., Robinson, L.F., Auro, M.E., Gagnon, A.C., 2010. Environmental and biological controls on Mg and Li in deep-
1059   sea scleractinian corals. Earth Planet. Sci. Lett. 300, 215–225. doi:10.1016/j.epsl.2010.09.029

1060 Castellan, G., Angeletti, L., Taviani, M., Montagna, P., 2019. The Yellow Coral Dendrophyllia cornigera in a Warming
1061   Ocean. Front. Mar. Sci. 6, 692. doi:10.3389/fmars.2019.00692

1062 Cheng, H., Adkins, J., Edwards, R.L., Boyle, E.A., 2000. U-Th dating of deep-sea corals. Geochim. Cosmochim. Acta 64,
1063   2401–2416. doi:10.1016/S0016-7037(99)00422-6

1064 Church, J.A., White, N.J., Aarup, T., Wilson, W.S., Woodworth, P.L., Domingues, C.M., Hunter, J.R., Lambeck, K., 2008.
1065   Understanding global sea-levels: Past, present and future. Sustain. Sci. 3, 9–22. doi:10.1007/s11625-008-0042-4

1066 Colantoni, P., 1973. A glacial mollusc fauna from Baronie Seamount (off eastern Sardinia). Rapp. Comm. int. Mer. Médit.
1067   21, 896–900.

1068 Colin, C., Frank, N., Copard, K., Douville, E., 2010. Neodymium isotopic composition of deep-sea corals from the NE
1069   Atlantic: Implications for past hydrological changes during the Holocene. Quat. Sci. Rev. 29, 2509–2517.
1070   doi:10.1016/j.quascirev.2010.05.012

1071 Comas, M., Pinheiro, L.M., 2010. The Melilla carbonate mounds: do deep-water coral mounds count on seeping fluids in the
1072   Alboran Sea? Rapp. Comm. int. Mer. Médit. 39, 16.

1073 Corbera, G., Lo Iacono, C., Gràcia, E., Grinyó, J., Pierdomenico, M., Huvenne, V.A.I., Aguilar, R., Gili, J.M., 2019.
1074   Ecological characterisation of a Mediterranean cold-water coral reef: Cabliers Coral Mound Province (Alboran Sea,
1075   western Mediterranean). Prog. Oceanogr. 175, 245–262. doi:10.1016/j.pocean.2019.04.010

1076 Correa, T., Grasmueck, M., Eberli, G.P., Reed, J.K., Verwer, K., Purkis, S.A.M., 2012. Variability of cold-water coral
1077   mounds in a high sediment input and tidal current regime, Straits of Florida. Sedimentology 59, 1278–1304.

1078 Davies, A.J., Duineveld, G.C.A., Lavaleye, M.S.S., Bergman, M.J.N., van Haren, H., Roberts, J.M., 2009. Downwelling and
1079   deep-water bottom currents as food supply mechanisms to the cold-water coral *Lophelia pertusa* (Scleractinia) at the
1080   Mingulay Reef Complex. Limnol. Oceanogr. 54, 620–629.

1081 De Haas, H., Mienis, F., Frank, N., Richter, T.O., Steinacher, R., De Stigter, H., der Land, C., Van Weering, T.C.E., 2009.
1082   Morphology and sedimentology of (clustered) cold-water coral mounds at the south Rockall Trough margins, NE
1083   Atlantic Ocean. Facies 55, 1–26.

1084 De Mol, B., Van Rensbergen, P., Pillen, S., Van Herreweghe, K., Van Rooij, D., McDonnell, A., Huvenne, V., Ivanov, M.,
1085   Swennen, R., Henriet, J.P., 2002. Large deep-water coral banks in the Porcupine Basin, southwest of Ireland. Mar.
1086   Geol. 188, 193–231. doi:10.1016/S0025-3227(02)00281-5

1087 De Mol, B., Henriet, J.-P., Canals, M., 2005. Development of coral banks in Porcupine Seabight: do they have
1088   Mediterranean ancestors? in: Cold-Water Corals and Ecosystems. Springer Berlin Heidelberg, pp. 515–533.
1089   doi:10.1007/3-540-27673-4_26

1090 Dorale, J.A., Onac, B.P., Fornós, J.J., Ginés, J., Ginés, A., Tuccimei, P., Peate, D.W., 2010. Sea-Level Highstand 81,000
1091   Years Ago in Mallorca. Science 327, 860–863. doi:10.1126/science.1181725

1092 Dorschel, B., Hebbeln, D., Rüggeberg, A., Dullo, W.C., Freiwald, A., 2005. Growth and erosion of a cold-water coral
1093   covered carbonate mound in the Northeast Atlantic during the Late Pleistocene and Holocene. Earth Planet. Sci. Lett.
1094   233, 33–44. doi:10.1016/j.epsl.2005.01.035

1095 Duggen, S., Hoernle, K., van den Bogaard, P., Harris, C., 2004. Magmatic evolution of the Alboran region: the role of
1096   subduction in forming the western Mediterranean and causing the Messinian Salinity Crisis. Earth Planet. Sci. Lett.
1097   218, 91–108.

1098 Eggins, S.M., Grün, R., McCulloch, M.T., Pike, A.W.G., Chappell, J., Kinsley, L., Mortimer, G., Shelley, M., Murray-
1099   Wallace, C. V., Spötl, C., Taylor, L., 2005. In situ U-series dating by laser-ablation multi-collector ICPMS: New
1100   prospects for Quaternary geochronology. Quat. Sci. Rev. 24, 2523–2538. doi:10.1016/j.quascirev.2005.07.006

1101 Eisele, M., Frank, N., Wienberg, C., Hebbeln, D., López Correa, M., Douville, E., Freiwald, A., 2011. Productivity
1102   controlled cold-water coral growth periods during the last glacial off Mauritania. Mar. Geol. 280, 143–149.
1103   doi:10.1016/j.margeo.2010.12.007

1104 Eisele, M., Frank, N., Wienberg, C., Titschack, J., Mienis, F., Beuck, L., Tisnerat-Laborde, N., Hebbeln, D., 2014.
1105   Sedimentation patterns on a cold-water coral mound off Mauritania. Deep. Res. Part II Top. Stud. Oceanogr. 99, 307–
1106   315. doi:10.1016/j.dsr2.2013.07.004

1107 Fabri, M.-C., Bargain, A., Pairaud, I., Pedel, L., Taupier-Letage, I., 2017. Cold-water coral ecosystems in Cassidaigne
1108   Canyon: An assessment of their environmental living conditions. Deep Sea Res. Part II Top. Stud. Oceanogr. 137,
1109   436–453.

1110 Filippidi, A., Triantaphyllou, M. V., De Lange, G.J., 2016. Eastern-Mediterranean ventilation variability during sapropel S1
1111   formation, evaluated at two sites influenced by deep-water formation from Adriatic and Aegean Seas. Quat. Sci. Rev.
1112   144, 95–106. doi:10.1016/j.quascirev.2016.05.024

1113 Fink, H.G., Wienberg, C., De Pol-Holz, R., Wintersteller, P., Hebbeln, D., 2013. Cold-water coral growth in the Alboran Sea
1114   related to high productivity during the Late Pleistocene and Holocene. Mar. Geol. 339, 71–82.

1115 Fink, H.G., Wienberg, C., De Pol-Holz, R., Hebbeln, D., 2015. Spatio-temporal distribution patterns of Mediterranean cold-
1116   water corals (*Lophelia pertusa* and *Madrepora oculata*) during the past 14,000 years. Deep. Res. Part I Oceanogr.
1117   Res. Pap. 103, 37–48. doi:10.1016/j.dsr.2015.05.006

1118 Foubert, A., Huvenne, V.A.I., Wheeler, A., Kozachenko, M., Opderbecke, J., Henriet, J.P., 2011. The Moira Mounds, small
1119   cold-water coral mounds in the Porcupine Seabight, NE Atlantic: Part B-Evaluating the impact of sediment dynamics
1120   through high-resolution ROV-borne bathymetric mapping. Mar. Geol. 282, 65–78. doi:10.1016/j.margeo.2011.02.008

1121   Frank, N., Freiwald, A., López Correa, M., Wienberg, C., Eisele, M., Hebbeln, D., Van Rooij, D., Henriet, J.P., Colin, C.,
1122   van Weering, T., de Haas, H., Buhl-Mortensen, P., Roberts, J.M., De Mol, B., Douville, E., Blamart, D., Hatté, C.,
1123   2011. Northeastern Atlantic cold-water coral reefs and climate. Geology 39, 743–746. doi:10.1130/G31825.1

1124   García Lafuente, J., Cano, N., Vargas, M., Rubín, J.P., Hernández-Guerra, A., 1998. Evolution of the Alboran Sea
1125   hydrographic structures during July 1993. Deep Sea Res. Part I Oceanogr. Res. Pap. 45, 39–65.

1126   Gori, A., Reynaud, S., Orejas, C., Ferrier-Pagès, C., 2015. The influence of flow velocity and temperature on zooplankton
1127   capture rates by the cold-water coral *Dendrophyllia cornigera*. J. Exp. Mar. Bio. Ecol. 466, 92–97.

1128   Gori, A., Reynaud, S., Orejas, C., Gili, J.M., Ferrier-Pagès, C., 2014. Physiological performance of the cold-water coral
1129   *Dendrophyllia cornigera* reveals its preference for temperate environments. Coral Reefs 33, 665–674.
1130   doi:10.1007/s00338-014-1167-9

1131   Grant, K.M., Grimm, R., Mikolajewicz, U., Marino, G., Ziegler, M., Rohling, E.J., 2016. The timing of Mediterranean
1132   sapropel deposition relative to insolation, sea-level and African monsoon changes. Quat. Sci. Rev. 140, 125–141.
1133   doi:10.1016/j.quascirev.2016.03.026

1134   Grant, K.M., Rohling, E.J., Bronk Ramsey, C., Cheng, H., Edwards, R.L., Florindo, F., Heslop, D., Marra, F., Roberts, A.P.,
1135   Tamisiea, M.E., Williams, F., 2014. Sea-level variability over five glacial cycles. Nat. Commun. 5, 1–9.
1136   doi:10.1038/ncomms6076

1137   Hauser, I., Oschmann, W., Gischler, E., 2008. Taphonomic Signatures On Modern Caribbean Bivalve Shells As Indicators
1138   Of Environmental Conditions (Belize, Central America). Palaios 23, 586–600. doi:10.2110/palo.2007.p07-075r

1139   Hebbeln, D., Wienberg, C., Beuck, L., Freiwald, A., Wintersteller, P., Cruise participants, n.d. Report and preliminary
1140   results of RV POSEIDON Cruise POS 385 "Cold-Water Corals of the Alboran Sea (western Mediterranean Sea)".
1141   Faro–Toulon, May 29–June 16, 2009. Berichte. Fachbereich Geowissenschaften. Universität Bremen. No. 273, 79 p.
1142   Bremen.

1143   Hebbeln, D., Wienberg, C., Wintersteller, P., Freiwald, A., Becker, M., Beuck, L., Dullo, C., Eberli, G.P., Glogowski, S.,
1144   Matos, L., Forster, N., Reyes-Bonilla, H., Taviani, M., 2014. Environmental forcing of the Campeche cold-water coral
1145   province, southern Gulf of Mexico. Biogeosciences 11, 1799–1815. doi:10.5194/bg-11-1799-2014

1146   Hebbeln, D., 2019. Highly Variable Submarine Landscapes in the Alborán Sea Created by Cold-Water Corals, in: Orejas, C.,
1147   Jiménez, C. (Eds.), Mediterranean Cold-Water Corals: Past, Present and Future. Springer, Cham, pp. 61–65.
1148   doi:10.1007/978-3-319-91608-8_8

1149   Hebbeln, D., Van Rooij, D., Wienberg, C., 2016. Good neighbours shaped by vigorous currents: Cold-water coral mounds
1150   and contourites in the North Atlantic. Mar. Geol. 378, 171–185. doi:10.1016/j.margeo.2016.01.014

1151   Hoffmann, D.L., Standish, C.D., García-Diez, M., Pettitt, P.B., Milton, J.A., Zilhão, J., Alcolea-González, J.J., Cantalejo-
1152   Duarte, P., Collado, H., De Balbín, R., Lorblanchet, M., Ramos-Muñoz, J., Weniger, G.C., Pike, A.W.G., 2018. U-Th
1153   dating of carbonate crusts reveals Neandertal origin of Iberian cave art. Science 359, 912–915.
1154   doi:10.1126/science.aap7778

1155   Holden, N.E., 1990. Total half-lives for selected nuclides. Pure Appl. Chem. 62, 941–958. doi:10.1351/pac199062050941

1156   Horwitz, E.P., Dietz, M.L., Chiarizia, R., 1992. The application of novel extraction chromatographic materials to the
1157   characterization of radioactive waste solutions. J. Radioanal. Nucl. Chem. 161, 575–583. doi:10.1007/BF02040504

1158   Hovland, M., Mortensen, P.B., 1999. Norske Korallrev Og Prosessor i Havbunnen. (Deep-water Coral-reefs and Processes
1159   on the Sea Floor). John Grieg Forlag.

1160   Huh, Y., Chan, L.H., Zhang, L., Edmond, J.M., 1998. Lithium and its isotopes in major world rivers: implications for
1161   weathering and the oceanic budget. Geochim. Cosmochim. Acta 62, 2039–2051. doi:10.1016/S0016-7037(98)00126-
1162   4

1163   Huvenne, V.A.I., De Mol, B., Henriet, J.P., 2003. A 3D seismic study of the morphology and spatial distribution of buried
1164   coral banks in the Porcupine Basin, SW of Ireland. Mar. Geol. 198, 5–25. doi:10.1016/S0025-3227(03)00092-6

1165   Jaffey, A.H., Flynn, K.F., Glendenin, L.E., Bentley, W.C., Essling, A.M., 1971. Precision measurement of half-lives and
1166   specific activities of U235 and U238. Phys. Rev. C 4, 1889–1906. doi:10.1103/PhysRevC.4.1889

1167   Jiménez-Espejo, F.J., Pardos-Gené, M., Martínez-Ruiz, F., García-Alix, A., van de Flierdt, T., Toyofuku, T., Bahr, A.,
1168   Kreissig, K., 2015. Geochemical evidence for intermediate water circulation in the westernmost Mediterranean over
1169   the last 20 kyr BP and its impact on the Mediterranean Outflow. Glob. Planet. Change 135, 38–46.
1170   doi:10.1016/j.gloplacha.2015.10.001

1171   Kampman, N., Burnside, N.M., Shipton, Z.K., Chapman, H.J., Nicholl, J.A., Ellam, R.M., Bickle, M.J., 2012. Pulses of
1172   carbon dioxide emissions from intracrustal faults following climatic warming. Nat. Geosci. 5, 352–358.
1173   doi:10.1038/ngeo1451

1174   Kano, A., Ferdelman, T.G., Williams, T., Henriet, J.-P., Ishikawa, T., Kawagoe, N., Takashima, C., Kakizaki, Y., Abe, K.,
1175   Sakai, S., others, 2007. Age constraints on the origin and growth history of a deep-water coral mound in the northeast
1176   Atlantic drilled during Integrated Ocean Drilling Program Expedition 307. Geology 35, 1051–1054.

1177   Kidwell, S.M., Holland, S.M., 1991. Field Description of Coarse Bioclastic Fabrics. Palaios 6, 426. doi:10.2307/3514967

1178   Konijnendijk, T.Y.M., Ziegler, M., Lourens, L.J., 2014. Chronological constraints on Pleistocene sapropeldepositions from
1179   high-resolution geochemicalrecords of ODP Sites 967 and 968. Newsletters Stratigr. 47, 263–282.

1180   Lambeck, K., Rouby, H., Purcell, A., Sun, Y., Sambridge, M., 2014. Sea-level and global ice volumes from the Last Glacial
1181   Maximum to the Holocene. Proc. Natl. Acad. Sci. U. S. A. 111, 15296–15303. doi:10.1073/pnas.1411762111

1182   Lo Iacono, C., Gracia, E., Agnastounou, E., Emelianov, M., Foster, G.L., Garcia-Ladona, E., Gili, J.M., Grinyo, J., Huvenne,
1183   V.A.I., Kastamemis, O.L., Mavrogordato, M.N., Perea, H., Pierdomenico, M., Vertino, A., Victorero-Gonzalez, L.,
1184   Van Rooij, D., 2016. Living reefs and DWC mounds in the Alboran Sea (Western Mediterranean): Holocene
1185   evolution and present-day conditions, in: 6 International Symposium on Deep-Sea Corals, 11.09.-16.09.2016. Boston,
1186   USA.

1187   Lo Iacono, C., Gràcia, E., Diez, S., Bozzano, G., Moreno, X., Dañobeitia, J., Alonso, B., 2008. Seafloor characterization and
1188   backscatter variability of the Almería Margin (Alboran Sea, SW Mediterranean) based on high-resolution acoustic
1189   data. Mar. Geol. 250, 1–18. doi:10.1016/j.margeo.2007.11.004

1190   Lo Iacono, C., Gràcia, E., Ranero, C.R., Emelianov, M., Huvenne, V.A.I., Bartolomé, R., Booth-Rea, G., Prades, J.,
1191   Ambroso, S., Dominguez, C., others, 2014. The West Melilla cold water coral mounds, Eastern Alboran Sea:
1192   Morphological characterization and environmental context. Deep Sea Res. Part II Top. Stud. Oceanogr. 99, 316–326.

1193   Lo Iacono, C., Savini, A., Basso, D., 2018. Cold-water carbonate bioconstructions, in: Submarine Geomorphology. Springer,
1194   pp. 425–455.

1195   Lo Iacono, C., Savini, A., Huvenne, V.A.I., Gràcia, E., 2019. Habitat Mapping of Cold-Water Corals in the Mediterranean
1196   Sea, in: Orejas, C., Jiménez, C. (Eds.), Mediterranean Cold-Water Corals: Past, Present and Future. Springer, Cham,
1197   pp. 157–171. doi:10.1007/978-3-319-91608-8_15

1198   López Correa, M., Freiwald, A., Hall-Spencer, J., Taviani, M., 2006. Distribution and habitats of *Acesta excavata* (Bivalvia:
1199   Limidae) with new data on its shell ultrastructure, in: Cold-Water Corals and Ecosystems. Springer-Verlag, pp. 173–
1200   205. doi:10.1007/3-540-27673-4_9

1201   Macías, D., Bruno, M., Echevarría, F., Vázquez, A., García, C.M., 2008. Meteorologically-induced mesoscale variability of
1202   the North-western Alboran Sea (southern Spain) and related biological patterns. Estuar. Coast. Shelf Sci. 78, 250–266.
1203   doi:10.1016/j.ecss.2007.12.008

1204   Martinez-Ruiz, F., Kastner, M., Gallego-Torres, D., Rodrigo-Gámiz, M., Nieto-Moreno, V., Ortega-Huertas, M., 2015.
1205   Paleoclimate and paleoceanography over the past 20,000yr in the Mediterranean Sea Basins as indicated by sediment
1206   elemental proxies. Quat. Sci. Rev. doi:10.1016/j.quascirev.2014.09.018

1207   Martorelli, E., Petroni, G., Chiocci, F.L., others, 2011. Contourites offshore Pantelleria Island (Sicily Channel,
1208   Mediterranean Sea): depositional, erosional and biogenic elements. Geo-Mar. Lett. 31, 481–493.

1209   Martrat, B., Grimalt, J.O., Lopez-Martinez, C., Cacho, I., Sierro, F.J., Flores, J.A., Zahn, R., Canals, M., Curtis, J.H., Hodell,
1210   D.A., 2004. Abrupt temperature changes in the Western Mediterranean over the past 250,000 years. Science 306,
1211   1762–1765. doi:10.1126/science.1101706

1212   McGregor, H. V., Hellstrom, J., Fink, D., Hua, Q., Woodroffe, C.D., 2011. Rapid U-series dating of young fossil corals by
1213   laser ablation MC-ICPMS. Quat. Geochronol. 6, 195–206. doi:10.1016/j.quageo.2010.10.002

1214   McManus, M., Alldredge, A., Barnard, A., Boss, E., Case, J., Cowles, T., Donaghay, P., Eisner, L., Gifford, D., Greenlaw,
1215   C., Herren, C., Holliday, D., Johnson, D., MacIntyre, S., McGehee, D., Osborn, T., Perry, M., Pieper, R., Rines, J.,
1216   Smith, D., Sullivan, J., Talbot, M., Twardowski, M., Weidemann, A., Zaneveld, J., 2003. Characteristics, distribution
1217   and persistence of thin layers over a 48 hour period. Mar. Ecol. Prog. Ser. 261, 1–19. doi:10.3354/meps261001

1218   Mienis, F., de Stigter, H.C., White, M., Duineveld, G., de Haas, H., van Weering, T.C.E., 2007. Hydrodynamic controls on
1219   cold-water coral growth and carbonate-mound development at the SW and SE Rockall Trough Margin, NE Atlantic
1220   Ocean. Deep. Res. Part I Oceanogr. Res. Pap. 54, 1655–1674. doi:10.1016/j.dsr.2007.05.013

1221   Mienis, F., van Weering, T., de Haas, H., de Stigter, H., Huvenne, V., Wheeler, A., 2006. Carbonate mound development at
1222   the SW Rockall Trough margin based on high resolution TOBI and seismic recording. Mar. Geol. 233, 1–19.
1223   doi:10.1016/j.margeo.2006.08.003

1224   Millot, C., 2009. Another description of the Mediterranean Sea outflow. Prog. Oceanogr. 82, 101–124.
1225   doi:10.1016/j.pocean.2009.04.016

1226   Montagna, P., McCulloch, M., Douville, E., López Correa, M., Trotter, J., Rodolfo-Metalpa, R., Dissard, D., Ferrier-Pagès,
1227   C., Frank, N., Freiwald, A., Goldstein, S., Mazzoli, C., Reynaud, S., Rüggeberg, A., Russo, S., Taviani, M., 2014.
1228   Li/Mg systematics in scleractinian corals: Calibration of the thermometer. Geochim. Cosmochim. Acta 132, 288–310.
1229   doi:10.1016/j.gca.2014.02.005

1230   Montagna, P., Taviani, M., 2019. Mediterranean Cold-Water Corals as Paleoclimate Archives, in: Orejas, C., Jiménez, C.
1231   (Eds.), Mediterranean Cold-Water Corals: Past, Present and Future. Springer, Cham, pp. 95–108. doi:10.1007/978-3-
1232   319-91608-8_11

1233   Naumann, M.S., Orejas, C., Ferrier-Pagès, C., 2013. High thermal tolerance of two Mediterranean cold-water coral species
1234   maintained in aquaria. Coral Reefs 32, 749–754. doi:10.1007/s00338-013-1011-7

1235   Naumann, M.S., Orejas, C., Ferrier-Pagès, C., 2014. Species-specific physiological response by the cold-water corals
1236   *Lophelia pertusa* and *Madrepora oculata* to variations within their natural temperature range. Deep. Res. Part II Top.
1237   Stud. Oceanogr. 99, 36–41. doi:10.1016/j.dsr2.2013.05.025

1238   Navarro, G., Vázquez, Á., Macías, D., Bruno, M., Ruiz, J., 2011. Understanding the patterns of biological response to
1239   physical forcing in the Alborán Sea (western Mediterranean). Geophys. Res. Lett. 38, L23606.
1240   doi:10.1029/2011GL049708

1241   Oguz, T., Macias, D., Garcia-Lafuente, J., Pascual, A., Tintore, J., 2014. Fueling plankton production by a meandering
1242   frontal jet: a case study for the Alboran Sea (Western Mediterranean). PLoS One 9, e111482.

1243   Orejas, C., Gori, A., Jiménez, C., Rivera, J., Kamidis, N., Abu Alhaija, R., Lo Iacono, C., 2019. Occurrence and distribution
1244   of the coral *Dendrophyllia ramea* in Cyprus insular shelf: Environmental setting and anthropogenic impacts. Deep.
1245   Res. Part II Top. Stud. Oceanogr. 164, 190–205. doi:10.1016/j.dsr2.2019.04.006

1246   Orejas, C., Gori, A., Lo Iacono, C., Puig, P., Gili, J.-M., Dale, M.R.T., others, 2009. Cold-water corals in the Cap de Creus
1247   canyon, northwestern Mediterranean: spatial distribution, density and anthropogenic impact. Mar. Ecol. Prog. Ser.
1248   397, 37–51.

1249   Osborne, A.H., Marino, G., Vance, D., Rohling, E.J., 2010. Eastern Mediterranean surface water Nd during Eemian sapropel
1250   S5: Monitoring northerly (mid-latitude) versus southerly (sub-tropical) freshwater contributions. Quat. Sci. Rev. 29,
1251   2473–2483. doi:10.1016/j.quascirev.2010.05.015

1252   Palomino, D., Alonso, B., Lo Iacono, C., Casas, D., D'Acremont, E., Ercilla, G., Gorini, C., Vazquez, J.T., 2015. Seamounts
1253   and Seamount-like Structures of the Alborán Sea, in: Wurz, M., Rovere, M. (Eds.), Atlas of the Mediterranean
1254   Seamounts and Seamount-like Structures. IUCN, International Union for Conservation of Nature, pp. 124–132.

1255   Price, D.M., Robert, K., Callaway, A., Lo Iacono, C., Hall, R.A., Huvenne, V.A.I., 2019. Using 3D photogrammetry from
1256   ROV video to quantify cold-water coral reef structural complexity and investigate its influence on biodiversity and
1257   community assemblage. Coral Reefs 38, 1007–1021. doi:10.1007/s00338-019-01827-3

1258   Raddatz, J., Titschack, J., Frank, N., Freiwald, A., Conforti, A., Osborne, A., Skornitzke, S., Stiller, W., Rüggeberg, A.,
1259   Voigt, S., Albuquerque, A.L.S., Vertino, A., Schröder-Ritzrau, A., Bahr, A., 2020. *Solenosmilia variabilis*-bearing
1260   cold-water coral mounds off Brazil. Coral Reefs 39, 69–83. doi:10.1007/s00338-019-01882-w

1261   Raddatz, J., Liebetrau, V., Trotter, J., Rüggeberg, A., Flögel, S., Dullo, W.C., Eisenhauer, A., Voigt, S., McCulloch, M.,

1262   2016. Environmental constraints on Holocene cold-water coral reef growth off Norway: Insights from a multiproxy

1263   approach. Paleoceanography 31, 1350–1367. doi:10.1002/2016PA002974

1264   Rebesco, M., Taviani, M., 2019. A Turbulent Story: Mediterranean Contourites and Cold-Water Corals, in: Mediterranean

1265   Cold-Water Corals: Past, Present and Future. Springer, Cham, pp. 35–46.

1266   Reed, J.K., 1980. Distribution and structure of deep-water *Oculina varicosa* coral reefs off central eastern Florida. Bull. Mar.

1267   Sci. 30, 667–677.

1268   Remia, A., Taviani, M., 2005. Shallow-buried Pleistocene *Madrepora*-dominated coral mounds on a muddy continental

1269   slope, Tuscan Archipelago, NE Tyrrhenian Sea. Facies 50, 419–425.

1270   Roberts, J.M., Wheeler, A.J., Freiwald, A., 2006. Reefs of the deep: the biology and geology of cold-water coral ecosystems.

1271   Science 312, 543–547.

1272   Roberts, J.M., Wheeler, A.J., Freiwald, A., Cairns, S.D., 2009. Cold-water corals: The biology and geology of deep-sea coral

1273   habitats, Cold-Water Corals: The Biology and Geology of Deep-Sea Coral Habitats. Cambridge University Press.

1274   doi:10.1017/CBO9780511581588

1275   Rocchini, R., 1983. *Acesta excavata* (Fabricius, 1779), nuovo ritrovamento in Mediterraneo. Boll. Malacol. 19, 83–84.

1276   Rogerson, M., Cacho, I., Jimenez-Espejo, F., Reguera, M.I., Sierro, F.J., Martinez-Ruiz, F., Frigola, J., Canals, M., 2008. A

1277   dynamic explanation for the origin of the western Mediterranean organic-rich layers. Geochem. Geophys. Geosyst. 9,

1278   7. doi:10.1029/2007GC001936

1279   Rohling, E.J., Cane, T.R., Cooke, S., Sprovieri, M., Bouloubassi, I., Emeis, K.C., Schiebel, R., Kroon, D., Jorissen, F.J.,

1280   Lorre, A., Kemp, A.E.S., 2002. African monsoon variability during the previous interglacial maximum. Earth Planet.

1281   Sci. Lett. 202, 61–75. doi:10.1016/S0012-821X(02)00775-6

1282   Rohling, E.J., Sprovieri, M., Cane, T., Casford, J.S.L., Cooke, S., Bouloubassi, I., Emeis, K.C., Schiebel, R., Rogerson, M.,

1283   Hayes, A., Jorissen, F.J., Kroon, D., 2004. Reconstructing past planktic foraminiferal habitats using stable isotope

1284   data: A case history for Mediterranean sapropel S5. Mar. Micropaleontol. 50, 89–123. doi:10.1016/S0377-

1285   8398(03)00068-9

1286   Roy-Barman, M., Pons-Branchu, E., Levier, M., Bordier, L., Foliot, L., Gdaniec, S., Ayrault, S., Garcia-Orellana, J.,

1287   Masque, P., Castrillejo, M., 2019. Barium during the GEOTRACES GA-04S MedSeA cruise: The Mediterranean Sea

1288   Ba budget revisited. Chem. Geol. 511, 431–440. doi:10.1016/j.chemgeo.2018.09.015

1289   Savini, A., Corselli, C., 2010. High-resolution bathymetry and acoustic geophysical data from Santa Maria di Leuca Cold

1290   Water Coral province (Northern Ionian Sea–Apulian continental slope). Deep Sea Res. Part II Top. Stud. Oceanogr.

1291   57, 326–344.

1292   Savini, A., Vertino, A., Marchese, F., Beuck, L., Freiwald, A., 2014. Mapping Cold-Water Coral Habitats at Different Scales

1293   within the Northern Ionian Sea (Central Mediterranean): An Assessment of Coral Coverage and Associated

1294   Vulnerability. PLoS ONE 9(1): e87108. doi: 10.1371/journal.pone.0087108

1295   Scholz, D., Mangini, A., Felis, T., 2004. U-series dating of diagenetically altered fossil reef corals. Earth Planet. Sci. Lett.

1296   218, 163–178. doi:10.1016/S0012-821X(03)00647-2

1297   Sierro, F.J., Hodell, D.A., Curtis, J.H., Flores, J.A., Reguera, I., Colmenero-Hidalgo, E., Bárcena, M.A., Grimalt, J.O.,

1298   Cacho, I., Frigola, J., Canals, M., 2005. Impact of iceberg melting on Mediterranean thermohaline circulation during

1299   Heinrich events. Paleoceanography 20, PA2019. doi:10.1029/2004PA001051

1300   Spooner, P.T., Chen, T., Robinson, L.F., Coath, C.D., 2016. Rapid uranium-series age screening of carbonates by laser

1301   ablation mass spectrometry. Quat. Geochronol. 31, 28–39. doi:10.1016/j.quageo.2015.10.004

1302   Spooner, P.T., Robinson, L.F., Hemsing, F., Morris, P., Stewart, J.A., 2018. Extended calibration of cold-water coral Ba/Ca

1303   using multiple genera and co-located measurements of dissolved barium concentration. Chem. Geol. 499, 100–110.

1304   doi:10.1016/j.chemgeo.2018.09.012

1305   Stalder, C., El Kateb, A., Vertino, A., Rüggeberg, A., Camozzi, O., Pirkenseer, C.M., Spangenberg, J.E., Hajdas, I., Van

1306   Rooij, D., Spezzaferri, S., 2018. Large-scale paleoceanographic variations in the western Mediterranean Sea during

the last 34,000 years: From enhanced cold-water coral growth to declining mounds. Mar. Micropaleontol. 143, 46–62. doi:10.1016/j.marmicro.2018.07.007

Stalder, C., Vertino, A., Rosso, A., Rüggeberg, A., Pirkenseer, C., Spangenberg, J.E., Spezzaferri, S., Camozzi, O., Rappo, S., Hajdas, I., 2015. Microfossils, a key to unravel cold-water carbonate mound evolution through time: Evidence from the Eastern Alboran Sea. PLoS One 10. doi:10.1371/journal.pone.0140223

Stalling, D., Westerhoff, M., Hege, H.-C., 2005. Amira: A highly interactive system for visual data analysis. Vis. Handb. 38, 749–767.

Stewart, J.A., Robinson, L.F., Day, R.D., Strawson, I., Burke, A., Rae, J.W.B., Spooner, P.T., Samperiz, A., Etnoyer, P.J., Williams, B., Paytan, A., Leng, M.J., Häussermann, V., Wickes, L.N., Bratt, R., Pryer, H., 2020. Refining trace metal temperature proxies in cold-water scleractinian and stylasterid corals. Earth Planet. Sci. Lett. 545, 116412. doi:10.1016/j.epsl.2020.116412

Stumpf, R., Frank, M., Schönfeld, J., Haley, B.A., 2010. Late Quaternary variability of Mediterranean Outflow Water from radiogenic Nd and Pb isotopes. Quat. Sci. Rev. 29, 2462–2472. doi:10.1016/j.quascirev.2010.06.021

Tamborrino, L., Wienberg, C., Titschack, J., Wintersteller, P., Mienis, F., Schroder-Ritzrau, A., Freiwald, A., Orejas, C., Dullo, W.C., Haberkern, J., Hebbeln, D., 2019. Mid-holocene extinction of cold-water corals on the namibian shelf steered by the Benguela oxygen minimum zone. Geology 47, 1185–1188. doi:10.1130/G46672.1

Taviani, M., Angeletti, L., Canese, S., Cannas, R., Cardone, F., Cau, A., Cau, A.B., Follesa, M.C., Marchese, F., Montagna, P., others, 2017. The "Sardinian cold-water coral province" in the context of the Mediterranean coral ecosystems. Deep Sea Res. Part II Top. Stud. Oceanogr. 145, 61–78.

Taviani, M., Angeletti, L., Foglini, F., Corselli, C., Nasto, I., Pons-Branchu, E., Montagna, P., 2019. U/Th dating records of cold-water coral colonization in submarine canyons and adjacent sectors of the southern Adriatic Sea since the Last Glacial Maximum. Prog. Oceanogr. 175, 300–308. doi:10.1016/j.pocean.2019.04.011

Taviani, M., Colantoni, P., 1979. Thanatocoenoses Wurmiennes associees aux coraux blancs. Rapp. Comm. int. Mer Médit. 24/26.

Terreni, G., Voliani, A., 1995. New finding of *Acesta excavata* (Fabricius, 1779) in the Northern Tyrrhenian Sea. Conchiglia 276, 13–14.

Thierens, M., Browning, E., Pirlet, H., Loutre, M.F., Dorschel, B., Huvenne, V.A.I., Titschack, J., Colin, C., Foubert, A., Wheeler, A.J., 2013. Cold-water coral carbonate mounds as unique palaeo-archives: The Plio-Pleistocene Challenger Mound record (NE Atlantic). Quat. Sci. Rev. 73, 14–30. doi:10.1016/j.quascirev.2013.05.006

Thierens, M., Titschack, J., Dorschel, B., Huvenne, V.A.I., Wheeler, A.J., Stuut, J.B., O'Donnell, R., 2010. The 2.6 Ma depositional sequence from the Challenger cold-water coral carbonate mound (IODP Exp. 307): Sediment contributors and hydrodynamic palaeo-environments. Mar. Geol. 271, 260–277. doi:10.1016/j.margeo.2010.02.021

Titschack, J., 2019. 10 Bathyal Corals Within the Aegean Sea and the Adjacent Hellenic Trench. Springer, Cham, pp. 85–94. doi:10.1007/978-3-319-91608-8_10

Titschack, J., Baum, D., De Pol-Holz, R., López Correa, M., Forster, N., Flögel, S., Hebbeln, D., Freiwald, A., 2015. Aggradation and carbonate accumulation of Holocene Norwegian cold-water coral reefs. Sedimentology 62, 1873–1898. doi:10.1111/sed.12206

Titschack, J., Fink, H.G., Baum, D., Wienberg, C., Hebbeln, D., Freiwald, A., 2016. Mediterranean cold-water corals - an important regional carbonate factory? Depos. Rec. 2, 74–96. doi:10.1002/dep2.14

Titschack, J., Fink, H.G., Baum, D., Wienberg, C., Hebbeln, D., Freiwald, A., 2016. Mediterranean cold-water corals - an important regional carbonate factory? Depos. Rec. 2, 74–96. doi:10.1002/dep2.14

Toucanne, S., Jouet, G., Ducassou, E., Bassetti, M.A., Dennielou, B., Angue Minto'o, C.M., Lahmi, M., Touyet, N., Charlier, K., Lericolais, G., Mulder, T., 2012. A 130,000-year record of Levantine Intermediate Water flow variability in the Corsica Trough, western Mediterranean Sea. Quat. Sci. Rev. 33, 55–73. doi:10.1016/j.quascirev.2011.11.020

Vacchi, M., Marriner, N., Morhange, C., Spada, G., Fontana, A., Rovere, A., 2016. Multiproxy assessment of Holocene relative sea-level changes in the western Mediterranean: Sea-level variability and improvements in the definition of the isostatic signal. Earth-Sci. Rev. doi:10.1016/j.earscirev.2016.02.002

1354 van Haren, H., 2014. Internal wave–zooplankton interactions in the Alboran Sea (W-Mediterranean). J. Plankton Res. 36,
1355   1124–1134. doi:https://doi.org/10.1093/plankt/fbu031

1356 Vandorpe, T., Wienberg, C., Hebbeln, D., Van den Berghe, M., Gaide, S., Wintersteller, P., Van Rooij, D., 2017. Multiple
1357   generations of buried cold-water coral mounds since the Early-Middle Pleistocene Transition in the Atlantic
1358   Moroccan Coral Province, southern Gulf of Cádiz. Palaeogeogr. Palaeoclimatol. Palaeoecol. 485, 293–304.
1359   doi:10.1016/j.palaeo.2017.06.021

1360 Vargas-Yáez, M., Plaza, F., García-Lafuente, J., Sarhan, T., Vargas, J.M., Vélez-Belchi, P., 2002. About the seasonal
1361   variability of the Alboran Sea circulation. J. Mar. Syst. 35, 229–248. doi:10.1016/S0924-7963(02)00128-8

1362 Vargas-Yáñez, M., García-Martínez, M.C., Moya, F., Balbín, R., López-Jurado, J.L., Serra, M., Zunino, P., Pascual, J., Salat,
1363   J., 2017. Updating temperature and salinity mean values and trends in the Western Mediterranean: The RADMED
1364   project. Prog. Oceanogr. 157, 27–46. doi:10.1016/j.pocean.2017.09.004

1365 Vermeesch, P., 2018. IsoplotR: A free and open toolbox for geochronology. Geosci. Front. 9, 1479–1493.
1366   doi:10.1016/j.gsf.2018.04.001

1367 Vertino, A., Corselli, C., 2019. Did Quaternary Climate Fluctuations Affect Mediterranean Deep-Sea Coral Communities?,
1368   in: Orejas, C., Jiménez, C. (Eds.), Mediterranean Cold-Water Corals: Past, Present and Future. Springer, Cham, pp.
1369   51–55. doi:10.1007/978-3-319-91608-8_6

1370 Vertino, A., Taviani, M., Corselli, C., 2019. Spatio-Temporal Distribution of Mediterranean Cold-Water Corals, in: Orejas,
1371   C., Jiménez, C. (Eds.), Mediterranean Cold-Water Corals: Past, Present and Future. Springer, Cham, pp. 67–83.
1372   doi:10.1007/978-3-319-91608-8_9

1373 Victorero, L., Blamart, D., Pons-Branchu, E., Mavrogordato, M.N., Huvenne, V.A.I., 2016. Reconstruction of the formation
1374   history of the Darwin Mounds, N Rockall Trough: How the dynamics of a sandy contourite affected cold-water coral
1375   growth. Mar. Geol. 378, 186–195. doi:10.1016/j.margeo.2015.12.001

1376 Volkov, D.L., Fu, L.-L., 2010. On the Reasons for the Formation and Variability of the Azores Current. J. Phys. Oceanogr.
1377   40, 2197–2220. doi:10.1175/2010JPO4326.1

1378 Wang, H., Lo Iacono, C., Wienberg, C., Titschack, J., Hebbeln, D., 2019. Cold-water coral mounds in the southern Alboran
1379   Sea (western Mediterranean Sea): Internal waves as an important driver for mound formation since the last
1380   deglaciation. Mar. Geol. 412, 1–18. doi:10.1016/j.margeo.2019.02.007

1381 Wheeler, A.J., Beyer, A., Freiwald, A., de Haas, H., Huvenne, V.A.I., Kozachenko, M., Olu-Le Roy, K., Opderbecke, J.,
1382   2007. Morphology and environment of cold-water coral carbonate mounds on the NW European margin. Int. J. Earth
1383   Sci. 96, 37–56. doi:10.1007/s00531-006-0130-6

1384 Wheeler, A.J., Kozachenko, M., Henry, L.A., Foubert, A., de Haas, H., Huvenne, V.A.I., Masson, D.G., Olu, K., 2011. The
1385   Moira Mounds, small cold-water coral banks in the Porcupine Seabight, NE Atlantic: Part A-an early stage growth
1386   phase for future coral carbonate mounds? Mar. Geol. 282, 53–64. doi:10.1016/j.margeo.2010.08.006

1387 Wheeler, A.J., Beyer, A., Freiwald, A., De Haas, H., Huvenne, V.A.I., Kozachenko, M., Olu-Le Roy, K., Opderbecke, J.,
1388   2007. Morphology and environment of cold-water coral carbonate mounds on the NW European margin. Int. J. Earth
1389   Sci. 96, 37–56.

1390 White, M., Dorschel, B., 2010. The importance of the permanent thermocline to the cold water coral carbonate mound
1391   distribution in the NE Atlantic. Earth Planet. Sci. Lett. 296, 395–402.

1392 Wienberg, C., 2019. A Deglacial Cold-Water Coral Boom in the Alborán Sea: From Coral Mounds and Species Dominance,
1393   in: Orejas, C., Jiménez, C. (Eds.), Mediterranean Cold-Water Corals: Past, Present and Future. Springer, Cham, pp.
1394   57–60. doi:10.1007/978-3-319-91608-8_7

1395 Wienberg, C., Frank, N., Mertens, K.N., Stuut, J.B., Marchant, M., Fietzke, J., Mienis, F., Hebbeln, D., 2010. Glacial cold-
1396   water coral growth in the Gulf of Cádiz: Implications of increased palaeo-productivity. Earth Planet. Sci. Lett. 298,
1397   405–416. doi:10.1016/j.epsl.2010.08.017

1398 Wienberg, C., Titschack, J., 2015. Framework-Forming Scleractinian Cold-Water Corals Through Space and Time: A Late
1399   Quaternary North Atlantic Perspective, in: Marine Animal Forests. Springer, Cham, pp. 1–34. doi:10.1007/978-3-319-
1400   17001-5_16-1

1401 Wienberg, C., Titschack, J., Freiwald, A., Frank, N., Lundälv, T., Taviani, M., Beuck, L., Schröder-Ritzrau, A., Krengel, T.,

1402   Hebbeln, D., 2018. The giant Mauritanian cold-water coral mound province: Oxygen control on coral mound

1403   formation. Quat. Sci. Rev. 185, 135–152. doi:10.1016/j.quascirev.2018.02.012

1404 Wilson, J.B., 1979. Patch development of the deep-water coral *Lophelia pertusa* (L.) on Rockall Bank. J. Mar. Biol. Assoc.

1405   United Kingdom 59, 165–177. doi:10.1017/S0025315400046257

1406 Wu, J., Filippidi, A., Davies, G.R., de Lange, G.J., 2018. Riverine supply to the eastern Mediterranean during last

1407   interglacial sapropel S5 formation: A basin-wide perspective. Chem. Geol. 485, 74–89.

1408   doi:10.1016/j.chemgeo.2018.03.037

1409 Ziegler, M., Tuenter, E., Lourens, L.J., 2010. The precession phase of the boreal summer monsoon as viewed from the

1410   eastern Mediterranean (ODP Site 968). Quat. Sci. Rev. 29, 1481–1490. doi:10.1016/j.quascirev.2010.03.011

1411

1412